EURAS JOURNAL OF ENGINEERING AND APPLIED SCIENCES

Editorial Board

Scientific Advisory Board

Contents

Research Article

DOI Numbers

Impact of Wind and Temperature on Covid-19 Outbreak: Investigatory Analysis ın India

Mimansha Agrawal, Ajinkya Deokate, Mamta Agrawal, Zafer Aslan

10.17932/EJEAS.2021.024/ejeas_v04i1001

Energy Efficiency and Interior Comfort of The Building with Passive Geothermal Heating ın Temperate Climate

Ismail Arroub, Ahmed Bahlaoui, Soufiane Belhouideg

10.17932/EJEAS.2021.024/ejeas_v04i1002

Detection of Retinopathy Diseases Using Convolutional Neural Network Based on Discrete Cosine Transform

Mouad Kabbouri, Ali Okatan

10.17932/EJEAS.2021.024/ejeas_v04i1003

Design of Microscope Illumination System Based on Led Light Source and Collimator Using Zemax Software

Ismahen Osmani, Fouad Lakhdari, Mohamed Loghrab, Mounir Bouchaour

10.17932/EJEAS.2021.024/ejeas_v04i1004

Computational Modeling of Cold Flow Characteristics of A Single Cylinder Internal Combustion Engine For Different Turbulence Models

İsmail Hakkı Savcı, M. Zafer Gül

10.17932/EJEAS.2021.024/ejeas_v04i1005

From The Editor

Euras Journal of Engineering and Applied Sciences (EJEAS), is a peer-reviewed academic journal, establishing a solid platform for all academicians, consultants, researchers, and those who have a strong interest in global current issues and trends in engineering and applied sciences. Euras Journal of Engineering and Applied Sciences is based on engineering and applied sciences; artificial intelligence, cybersecurity, environmental sciences, food and food safety, biotechnology, material science and composites, nanotechnology, energy technologies, electronics, robotics, thermal sciences, earthquakes – structures – foundation and earth sciences studies. Subject areas could be as narrow as a specific phenomenon or device or as broad as a system.

EJEAS was established with the intention of promoting scholarly communication all over the world in a more effective manner. Our aim is to establish a publication that will be abstracted and indexed in the Engineering Index (EI) and Science Citation Index (SCI) in the near future. The journal has a short processing period to encourage young scientists.

Prof. Dr. Hasan HEPERKAN
Editor

IMPACT OF WIND AND TEMPERATURE ON COVID-19 OUTBREAK: INVESTIGATORY ANALYSIS IN INDIA

Mimansha Agrawal[1], Ajinkya Deokate[2],
Mamta Agrawal[3], Zafer Aslan[4]

[1,2,3]*VIT Bhopal University Madhya Pradesh India- 466114,*
[4]*Istanbul Aydin University, Istanbul, Turkey*
*mimanshaagrawal1998@gmail.com , drakage743@gmail.com
,mamta.agrawal@vitbhopal.ac.in , zaferaslan@aydin.edu.tr ,
0000-0001-7545-390X, 0000-0001-9302-4607, 0000-0001-5738-3450,
0000-0001-7707-7370*

ABSTRACT

The number of infected cases of COVID-19 has risen to over 100 million. With a recovery rate of 72.9% and a mortality rate of 2.2%. Although the safety measures, such as the protective face masks (PFMs) and social distancing, have been implemented, there was an explosion of infected cases in India over the span of 6 months in 2020, that is, May to October; under accordance with the arrival of monsoon. The virus spread shows preference to low temperatures and wind speed, as seen throughout India. Here, the study will shed light on the link between the spread of the pandemic in India and the meteorological factors of air temperature and wind speed. Weather data across state capitals and major cities is studied along with nation-wide data on COVID-19 infection cases. The study depicts the behavior of a variant of coronavirus in India, as less stable and low transmission rates at high temperatures and lower wind speeds. On the other hand, its stability, transmission and infection severity are considerably higher at lower temperatures and wind speed. The study traces the importance of self-isolation and social distancing, especially during cold weather conditions.

Keywords: SARS-CoV-2, Coronavirus, COVID-19, Meteorological Factors

1. INTRODUCTION

The pandemic of the coronavirus (COVID-19), also called the severe acute respiratory syndrome 2 (SARS-CoV-2) has devastated the economy of the world. Industries, the corporate sector, education and almost every other way of life has come to a standstill. The first encounter of this virus with humanity took place in China, in a city called Wuhan, in December 2019. The virus is named "Severe Acute Respiratory Syndrome Coronavirus 2 (SARS-CoV-2) by the International Committee on Taxonomy of Viruses (ICTV), as it is genetically related to the coronavirus responsible for the SARS outbreak of 2003. Since then, it has spread all over the globe and has been titled a pandemic by the World Health Organization (WHO).

As of January 1st, 2021, there have been 83743729 infected cases, 1824202 deaths, and 58796613 recovery cases reported globally. And India has a share of 10303409 infected, 149205 deaths, and 9901929 recovery cases (https://epidemicstats.com/coronavirus). There have been many safety protocols implemented throughout the country to prevent human-to-human transmission. These measures are put-forth to decrease transmission through the country, which might have been influenced by meteorological factors [7]. There have been many studies that have examined the relationship between coronavirus and meteorological factors, such as humidity [8], temperature [9], and air pollution [18], there is also the study done by Sarkodie and Owusu, which focuses on wind speed, surface pressure, precipitation and other meteorological factors (2020). The COVID-19 has shown a genetic variability due to which it has mutated during its time [19].

The WHO has reported four variants of the coronavirus, out of which, the one extracted in India is the UK variant. This study will focus on the meteorological factors of wind speed and temperature and their effects on the pandemic. The study will examine the number of infected cases along with the changes in weather conditions of India, and provide clarity on the effects of temperature and speed of winds on the pandemic.

2. METHODOLOGY

Using national-level data on each month and comparing the fluctuations in temperature and wind speed with cases of infections, the study will construct a data structure. Cities of Mumbai, Delhi, Ranchi, Kochi, Patna, Bilaspur, Jaipur, Bhopal, Chennai, Hyderabad, Shimla, Chandigarh,

Kolkata, Ahmedabad, Guwahati, Bhubaneswar (old), Dehradun, Lucknow, Puducherry, and Gangtok are taken under consideration for weather analysis throughout the affected states of India. For better investigation, all the considered cities are divided in four different parts of India i.e. Northern cities (Chandigarh, Shimla, Lucknow, Dehradun and Delhi), Eastern cities (Bhubaneswar, Gangtok, Ranchi, Guwahati and Patna), Southern cities (Puducherry, Visakhapatnam, Kochi, Mumbai, and Chennai), Western and Central cities (Jaipur, Bhopal, Jabalpur, and Bilaspur). The scarcely affected regions having consistent weather throughout the year are to be discarded for better analysis of fluctuating weather conditions. Weather parameters of temperature (max. & min. °C) and wind speed (km/hr), considered under the time frame of April 1st, 2020 to December 31st, 2020, are used for comparison with numbers of infection cases.
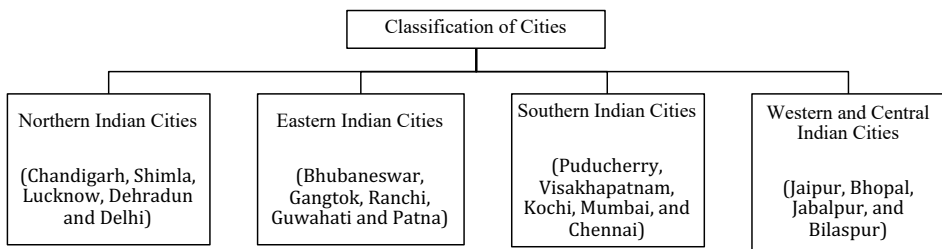
Figure 1. Classification of all the Cities used for the study of Wind Speed and Temperature

3. MATERIALS

The data used in this study has been taken from Weather Data Services | Visual Crossing, Weather Atlas (www.weather-atlas.com) for temperature and Epidemic Stats (https://epidemicstats.com/coronavirus) for statistics on COVID-19 cases and Weather Online (www.weatheronline.in) for wind speed, with data maps for COVID-19 cases from Wikipedia and OurWorldInData.org (https://ourworldindata.org/coronavirus-data). The temperature data consists of: Average temperatures, taken from April 1st, 2020 to December 31st, 2020. And the wind speed data consists of: Average wind speeds, for the same range.

The COVID-19 cases data (collected at the ends of the months) comprises of April, infected – 34862, deaths – 1154, recovered – 9068; May, infected – 190609, deaths – 5408, recovered – 91852; June, infected – 585792, deaths – 17410, recovered – 347836; July, infected – 169705, deaths – 36551, recovered – 1095647; August, infected – 3687939, deaths – 65435, recovered – 2837377; September, infected – 6310267, deaths – 98708,

recovered – 5270007; October, infected – 8136166, deaths – 122149, recovered – 7489203; November, infected – 9463254, deaths – 137659, recovered – 8888595; December, infected – 10286329, deaths – 149018, recovered – 9881786.

Table 1. Data considered for the Investigation

Data Category	Dates Taken		Units Used
	From	To	
Temperature	1st April, 2020	31st December, 2020	Degree Celsius (symbol: °C)
Wind Speed (Average)	1st April, 2020	31st December, 2020	Km/Hr.

4. DATA MODEL AND RESULTS

COVID-19 cases:
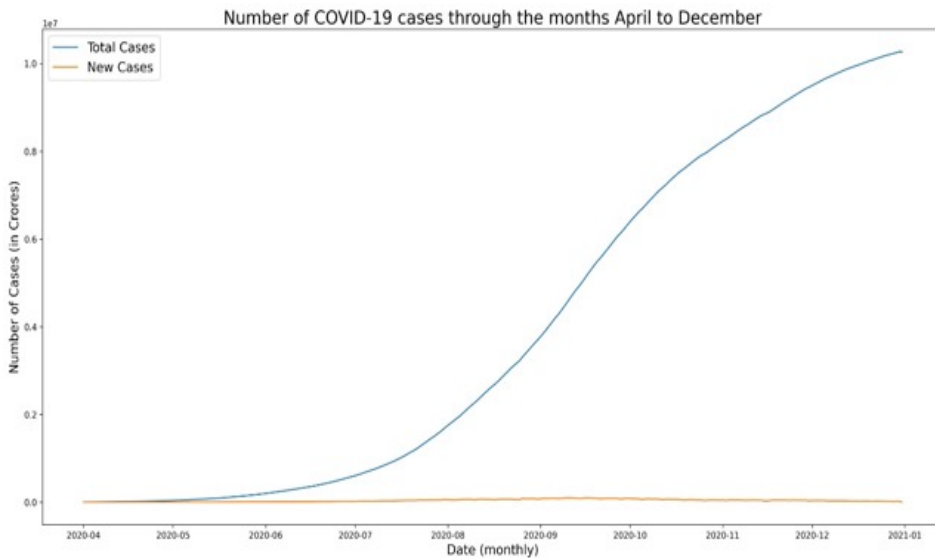
Figure 2. shows the number of COVID-19 cases through the months April to December of 2020, in India. Source: OurWorldInData

The number of COVID-19 cases show a steady incline till the month of August, where it starts increasing exponentially till October, and show a steady incline again afterwards. This is in accordance with the fall of temperatures and wind speed after the initial months of monsoon. The onset of the pandemic in India, came at the end of the month of March, April and may were plagued with steady increase of COVID-19 cases. The cases started increasing exponentially with the beginning of monsoon and lockdown relaxation in the months of August and September, and stabilizing in the winter.

A. Monthly Average Maximum and Minimum Temperatures:

I. For Eastern Indian Cities
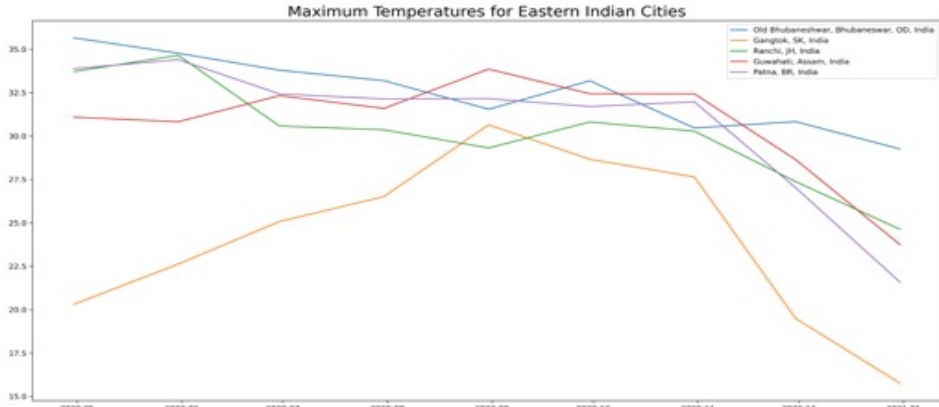
Fig 3. (a)
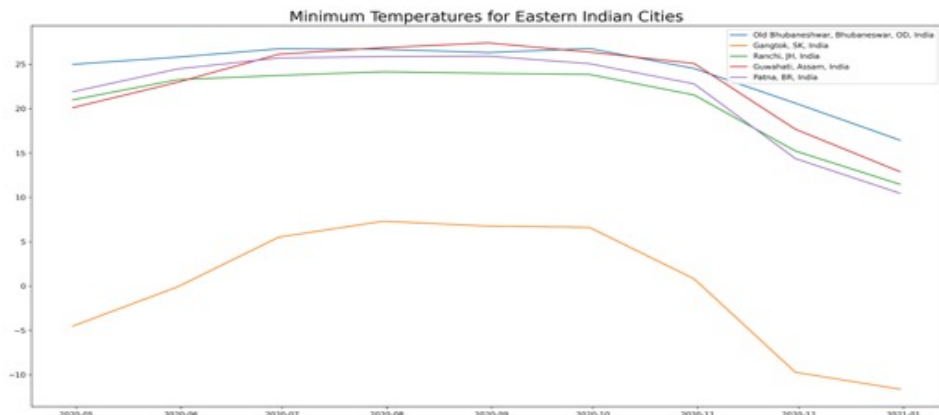
Fig 3. (b)

Figure 3. (a) and (b) show maximum and minimum monthly average temperatures for the cities of Bhubaneswar, Gangtok, Ranchi, Guwahati and Patna (Eastern Indian Cities)

Fig 3. Shows max and min monthly averaged temperatures of East Indian Cities. The maximum temperature lies between 35 ^{o}C to 20 ^{o}C and minimum temperature from 25 ^{o}C to 20 ^{o}C. As these cities lies in the eastern part of India, which means many of them are costal and hilly cities, due to which the temperature remains in this range and do not show much rise. Bhubaneshwar hold a steady minimum temperature of 26.63^{o}C and declining max. temperature from 34.7 to 33.1^{o}C over monsoon. Ranchi holds a steady minimum temperature of 23.92^{o}C and maximum temperature of 30.26^{o}C. Patna holds a minimum temperature of 25.63^{o}C and the maximum temperature declines from 32.42 to 31.7^{o}C. Guwahati

and Gangtok both show an exception to the temperature decline and fluctuations with both reaching their highest temperatures in the month of September. However, Gangtok depicts low temperatures throughout the year due to its geographical location, and thus the implied exception becomes irrelevant.

II. For Northern Indian Cities
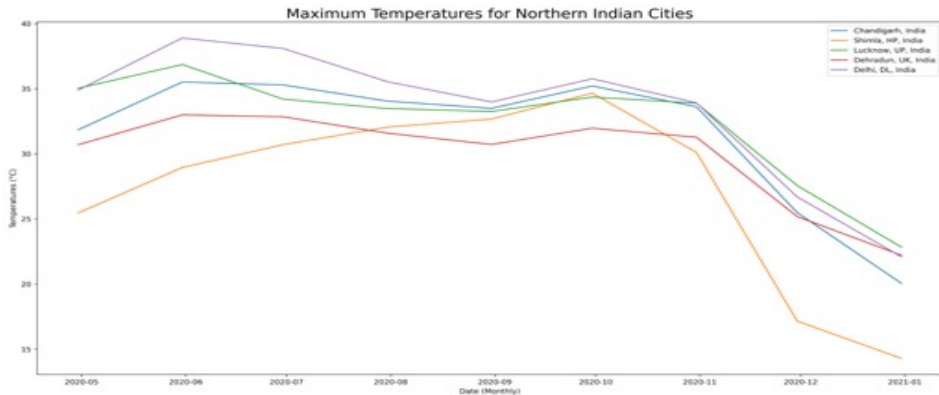
Fig 4. (a)
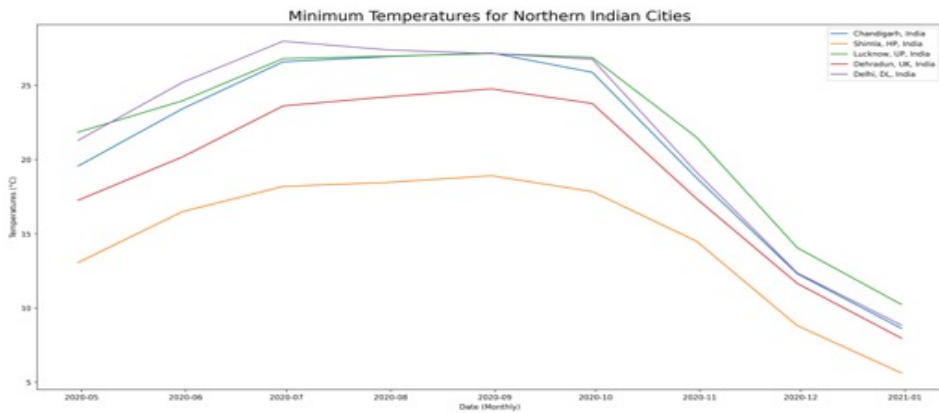
Fig 4. (b)

Figure 4. (a) and (b), depicts maximum and minimum average monthly temperatures for the cities of Chandigarh, Shimla, Lucknow, Dehradun and Delhi. (Northern Indian Cities)

Fig 4. Shows max and min monthly averaged temperatures of North Indian Cities. The maximum temperature lies between 38 °C to 25 °C and minimum temperature from 28 °C to 15 °C. As these cities lies in the northern part of India, most of the cities are highly populated, hilly and away from coast, hence due to which temperature in summer months is comparatively greater than in winter months. The temperature in early winter months

like October and November shows a peak, due to the offset of Monsoon and rise of humidity. Chandigarh showed decline in both maximum and minimum temperatures, with initial temperatures at 35.29^{o}C and 26.59^{o}C declining to 33.61^{o}C and 18.77^{o}C respectively. Lucknow and Delhi show similar trends to Chandigarh. Dehradun shows steady temperatures for both maximum and minimum, with minor fluctuations. Shimla shows an exception as it reaches its highest temperatures during monsoon.

III. For Northern Indian Cities
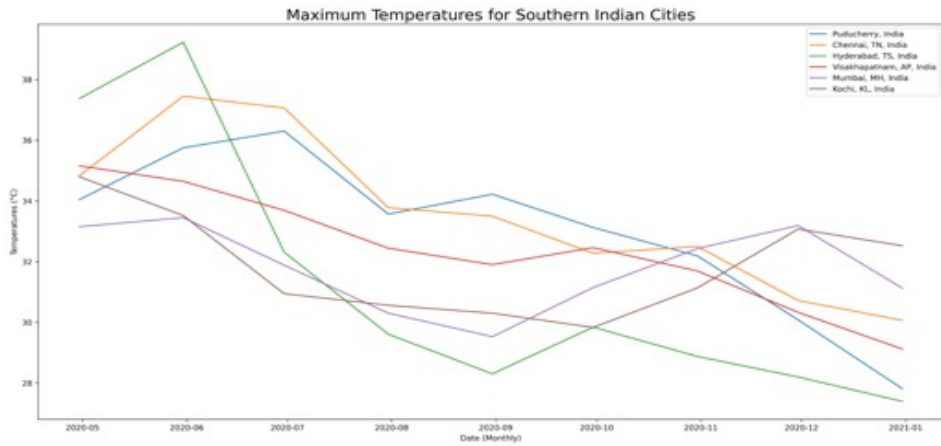
Fig 5. (a)
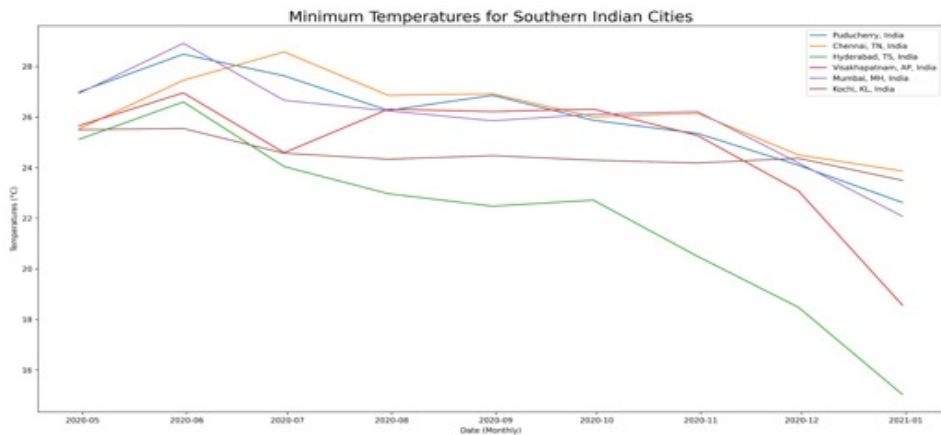
Fig 5. (b)

Figure 5. (a) and (b), depicts maximum and minimum monthly average temperatures for the cities of Puducherry, Visakhapatnam, Kochi, Mumbai, and Chennai. (Southern Indian Cities)

Fig 5. Shows max and min monthly averaged temperatures of North Indian Cities. The maximum temperature lies between 38°C to 30°C and minimum temperature from 28°C to 25°C. As these cities lies in the southern part

of India, the cities are mostly close to coast of India. The coastal cities relatively have moderate temperature and high humidity. The temperature is controlled by the humidity in these cities. During monsoon months the humidity is approximately near to null, due to which the maximum temperature falls. Puducherry, Vishakhapatnam, Kochi, Mumbai and Chennai without exception show drop in temperatures during monsoon with Hyderabad showing extreme drops. Also, one of the factors which can be considered is, these cities have various manufacturing industries which also rises the temperature.

IV. For Northern Indian Cities
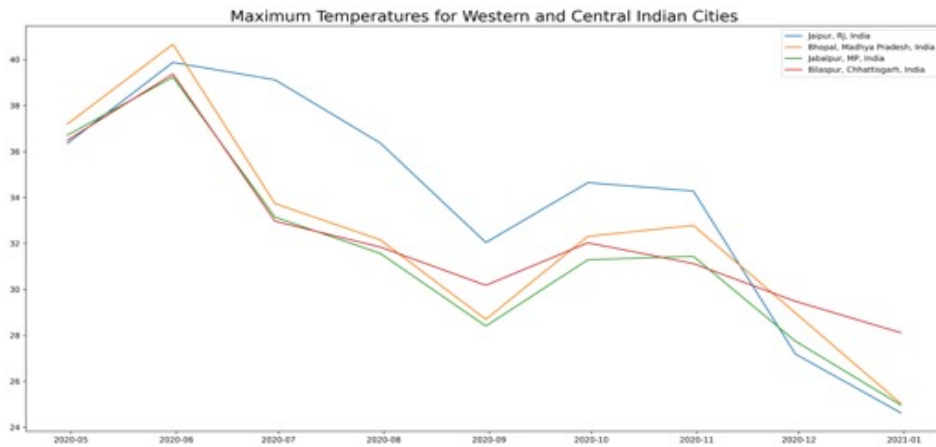
Fig 6. (a)
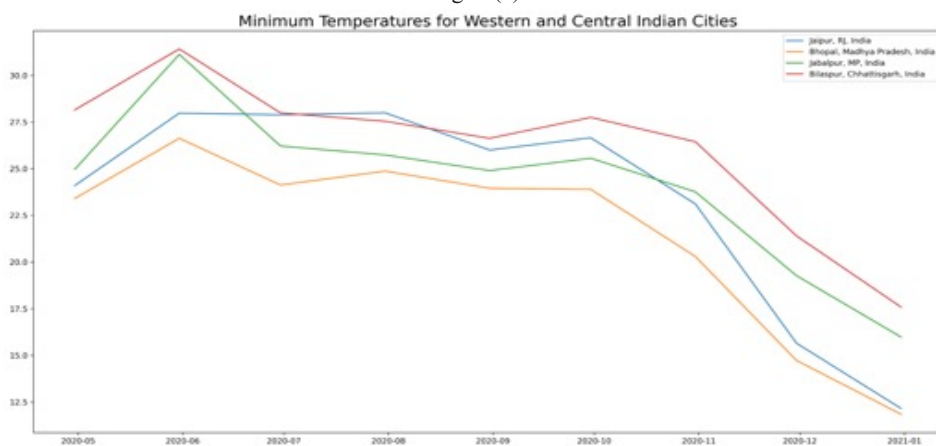
Fig 6. (b)

Figure 6. (a) and (b), depicts maximum and minimum monthly average temperatures for the cities of Jaipur, Bhopal, Jabalpur, and Bilaspur. (Western and Central Indian Cities)

Fig 6. Shows max and min monthly averaged temperatures of North Indian Cities. The maximum temperature lies between 38 °C to 30 °C and minimum temperature from 28 °C to 25 °C. As these cities lies in the western and central part of India, they are densely populated, plain cities and central cities. In the months of May and June, the temperature shows a rise, as the monsoon reaches the central and western regions little late as compared to the rest part of India. The onset of monsoon is marked in the months of late July till the beginning of October. Hence the temperature remains to be slightly less than the other months. Bilaspur, Jaipur, Jabalpur and Bhopal Show decline in both maximum and minimum temperatures after the onset of monsoon. Late October and November relatively experiences a high humid environment.

B. Monthly Average Wind Speed:
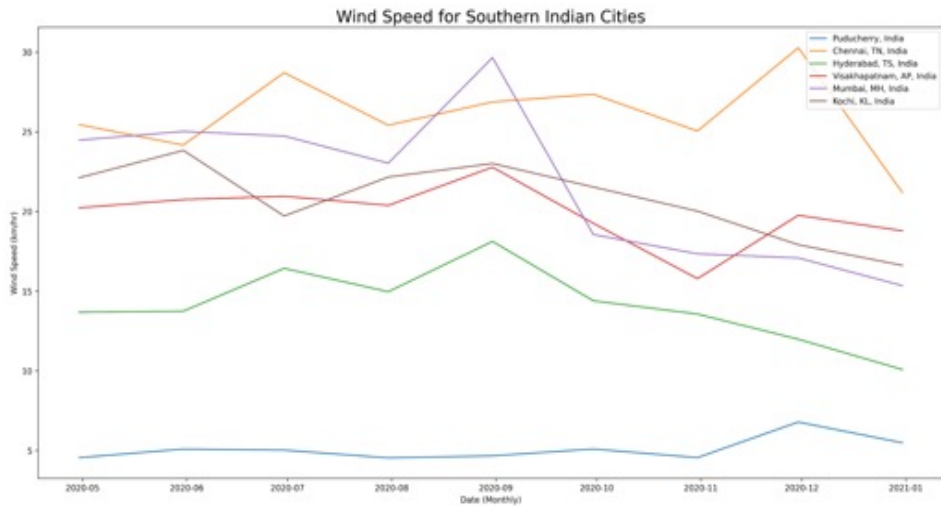
Fig 7. (a)
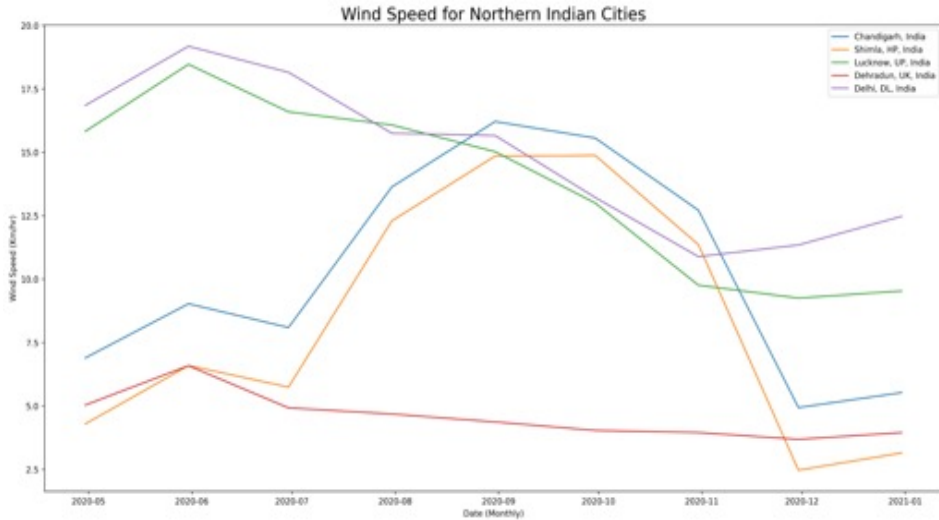
Fig 7. (b)

Shimla, Chandigarh, Mumbai and Chennai show unusual temperature trends, that spike in the middle months and then stabilize in the Winter period. The month of September shows the most unusual behavior, Chennai has a temperature spike even in the Winter.
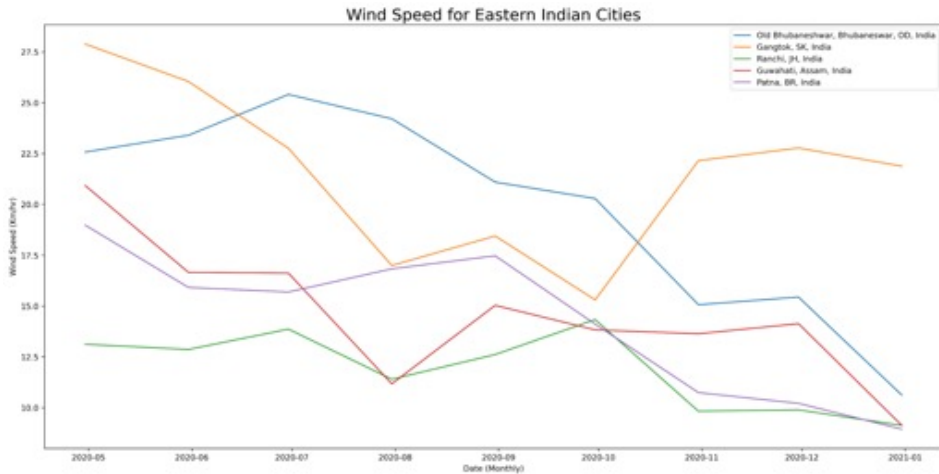
Fig 7. (c)
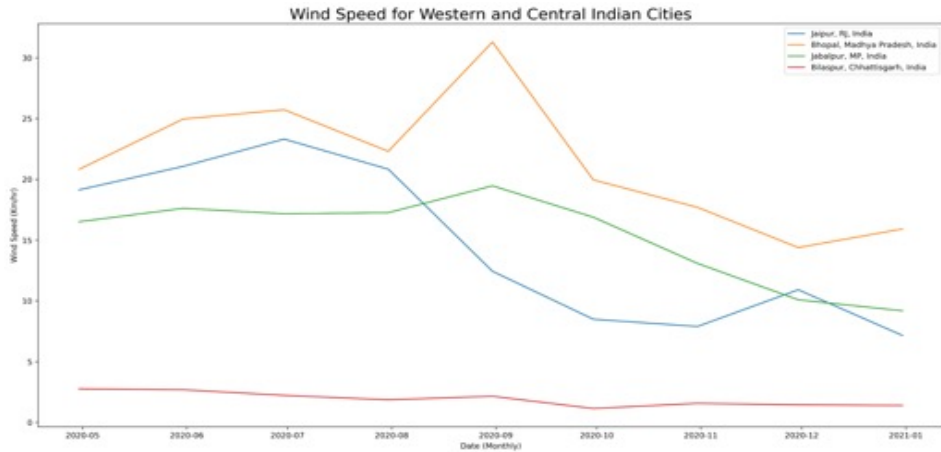
Fig 7. (d)

Figure 7. (a), (b), (c) and (d) depicts monthly average wind speed for the Indian cities.

The lowest average wind speed came in September for Chhattisgarh, an average of only 1.14 km/h. While the highest monthly wind speed average was for Bhopal, an average of 31.3 km/h. The majority of the cities show a decline from June to September, the monsoon season, with a momentary rise in June and July and a steep drop in August in some cities. The only exceptions are Shimla, Gangtok, Chennai and Puducherry, forming four exceptions out of twenty cities with Puducherry showing low temperatures throughout the year.

India experiences Summer in the months of April and May and monsoon from June to September. Therefore, it is a given that the cities will experience a decrease in both maximum and minimum temperatures. With only exceptions of Shimla, Gangtok and Assam. Which due to topographical factors, witness a rise in maximum temperatures(average). It is important to note that the cities showing exceptions (viz. Shimla, Guwahati, Gangtok) never showed greater temperatures than other cities during the concerned period, i.e. other cities always had higher temperatures than the cities in question. By comparing the above data, we can clearly see that as there is a drop in the temperature and wind speed, there is an exponential increase in the number of COVID cases. We can see a steep decrease in temperature in August and a corresponding increase in the number of infected people. There is a good recovery rate of 97.1% as of February 2021, but a steady death rate of 1.4%. Through the studied data given above from April to December 2020, a total of 10266674 people was infected.

5. DISCUSSION

High temperatures have shown to reduce the spread of COVID-19, whereas low temperatures are reported to facilitate the transmission of coronavirus [6]. Several studies report a rapid decline and viability of coronaviruses, such as the Middle East Respiratory Syndrome (MERS–Cov) and severe acute respiratory syndrome coronavirus (SARSCoV) at high temperatures [2,14]. The virus seemingly stabilizes in cold and dry climatic conditions, whereas warm and wet climatic conditions seems to help in reduction of Covid-19 spread, but these variables alone have been insufficient in explaining the transmission rates of the virus. Altamimi et al. [23] have found that MERS-CoV, in Saudi Arabia, prefers warmer weather conditions. Change in temperature, wind speed and humidity were meteorological variables that could affect SARS-Cov-1 transmission. According to the report released by the WHO there are currently four variants of COVID or SARS-CoV-2 circulating around the globe. The newer variants are supposedly more dangerous, but there is no clear evidence that they are causing increasingly severe outcomes. The variant found in India is the UK variant, which is less stable, viable and has lesser chances of transmission at higher temperatures and wind speed, and is more stable in lower temperature and wind speed, as shown in our study. Therefore, it is recommended that self-isolation and social distancing be practiced, along with other safety measures, especially during cold and rainy weather conditions.

6. CONCLUSION

The study has tried to clarify the effects of air temperature and speed on the pandemic situation. We collected the data through various modes and formed a link, which shows a relation between the fluctuations of meteorological factors and the spread of the coronavirus. By analyzing the data on temperature and wind speed, we can conclude that lesser temperature and lower wind speed causes the virus to concentrate at a place and causes the increase of infection cases. It also affects the recovery rate as recovery rates are seen to be higher at higher temperatures. Therefore, it is clear that the arrival of the monsoon and the drop-in temperature and wind speed had a negative impact on the pandemic situation in India.

7. LIMITATIONS

a. With temperature and wind speed there are also other meteorological factors that affect the pandemic, therefore it is difficult to reach a point of certainty.

b. There are also different variants of coronavirus that react differently to different weather conditions, so it is necessary to gather enough genetic evidence before reaching a concrete conclusion.

c. Various cultural and sociological factors also interfere in data analysis, as they affect the spread of the pandemic to a large extent.

REFERENCES

[1] Casanova LM, Jeon S, Rutala WA, Weber DJ, Sobsey MD, "Effects of air temperature and relative humidity on coronavirus survival on surfaces," Appl Environ Microbiol. 2010 May;76(9):2712-7. doi: 10.1128/AEM.02291-09. Epub 2010 Mar 12. PMID: 20228108; PMCID: PMC2863430.

[2] Chan KH, Peiris JS, Lam SY, Poon LL, Yuen KY, Seto WH, "The Effects of Temperature and Relative Humidity on the Viability of the SARS Coronavirus," Adv Virol. 2011;2011:734690. doi: 10.1155/2011/734690. Epub 2011 Oct 1. PMID: 22312351; PMCID: PMC3265313.

[3] CDC COVID-19 Response Team, "Preliminary Estimates of the Prevalence of Selected Underlying Health Conditions Among Patients with Coronavirus Disease 2019," - United States, February 12-March 28, 2020. MMWR Morb Mortal Wkly Rep. 2020 Apr 3;69(13):382-386. doi: 10.15585/mmwr.mm6913e2. PMID: 32240123; PMCID: PMC7119513.

[4] Christopher Fuhrmann, "The_Effects_of_Weather_and_Climate_on_ the_Seasonality_of_Influenza_What_We_Know_and_What_We_Need_ to_Know,".https://www.researchgate.net/publication/227628942, Accessed 2010.

[5] Grant WB, Lahore H, McDonnell SL, Baggerly CA, French CB, Aliano JL, et al., "Evidence that Vitamin D Supplementation Could Reduce Risk of Influenza and COVID-19 Infections and Deaths," Nutrients. 2020 Apr 2;12(4):988. doi: 10.3390/nu12040988. PMID: 32252338; PMCID: PMC7231123.

[6] Le, H.P., Sarkodie, S.A., "Dynamic linkage between renewable and conventional energy use, environmental quality and economic growth: evidence from Emerging Market and Developing Economies," Energy Rep. 6, 965–973, 2020.

[7] Li Q, Guan X, Wu P, Wang X, Zhou L, Tong Y, et al., "Early Transmission Dynamics in Wuhan, China, of Novel CoronavirusInfected Pneumonia," N Engl J Med. 2020 Mar 26;382(13):1199-1207. doi: 10.1056/NEJMoa2001316. Epub 2020 Jan 29. PMID: 31995857; PMCID: PMC7121484.

[8] Liu J, Zhou J, Yao J, Zhang X, Li L, Xu X, et al., "Impact of meteorological factors on the COVID-19 transmission: A multi-city study in China," Sci Total Environ. 2020 Jul 15;726:138513. doi: 10.1016/j. scitotenv.2020.138513. Epub 2020 Apr 9. PMID: 32304942; PMCID: PMC7194892.

[9] Ma Y, Zhao Y, Liu J, He X, Wang B, Fu S, et al., "Effects of temperature variation and humidity on the death of COVID-19 in Wuhan, China," Sci Total Environ. 2020 Jul 1;724:138226. doi: 10.1016/j. scitotenv.2020.138226. Epub 2020 Mar 26. PMID: 32408453; PMCID: PMC7142681.

[10] NASA, 2020. Meteorological Data Sets. Retrieved from. https:// nasa.gov.Pesaran, M.H., 2004. General Diagnostic Tests for Cross Section Dependence in Panels. Pesaran, M.H., 2007. A simple panel unit root test in the presence of cross-section dependence. J. Appl. Econom. 22, 265–312.

[11] Pesaran, M.H., Im, K.S., Shin, Y., "Testing for unit roots in heterogeneous panels," J. Econom. 115, 53–74, 2003.

[12] Sarkodie SA, Owusu PA., "Global assessment of environment, health and economic impact of the novel coronavirus (COVID-19)," Environ Dev Sustain. 2020 Jun 5:1-11. doi: 10.1007/s10668-020-00801-2. Epub ahead of print. PMID: 32837273; PMCID: PMC7272320.

[13] Sarkodie, S.A., Owusu, P.A., 2020b, "Investigating the cases of novel coronavirus disease (COVID-19) in China using dynamic statistical techniques," Heliyon 6, e03747.

[14] Van Doremalen, N., Bushmaker, T., Munster, V., "Stability of Middle East respiratory syndrome coronavirus (MERS-CoV) under different environmental conditions," Euro Surveill. 18, 20590, 2013.

[15] WHO, Novel Coronavirus (2019-nCoV) - Situation Report – 1. SITUATION REPORT - 1. Retrieved from.https://www.who.int/docs/defaultsource/coronaviruse/situation-reports/20200121-sitrep-1-2019-ncov.pdf? sfvrsn=20a99c10_4, 2020.

[16] Wilder-Smith, A., Freedman, D., "Isolation, quarantine, social distancing and community containment: pivotal role for old-style public health measures in the novel coronavirus (2019-nCoV) outbreak," J. Trav. Med. 27 taaa020, 2020.

[17] Xie, J., Zhu, Y., "Association between ambient temperature and COVID-19 infection in 122 cities from China," Sci. Total Environ. 724, 138201, 2020.

[18] Zhu, Y., Xie, J., Huang, F., Cao, L., "Association between short-term exposure to air pollution and COVID-19 infection: evidence from China," Sci. Total, 2020.

[19] Martinez MA., "Compounds with Therapeutic Potential against Novel Respiratory 2019 Coronavirus. Antimicrob Agents Chemother," 2020 Apr 21;64(5):e00399-20. doi: 10.1128/AAC.00399-20. PMID: 32152082; PMCID: PMC7179632.

[20] Sarkodie, S.A., Owusu, P.A., "Impact of meteorological factors on Covid19 pandemic: Evidence from top 20 countries with confirmed cases," 2020.

[21] Muhammad Rendana, "Impact of the wind conditions on Covid-19 pandemic: A new insight for the direction of the spread of the virus," 2020.

[22] Zhenkun Tian, Chiuxiang Yi, Yingying Fu, Jacqueline Singer, Qin Zhang, "Spatiotemporal analysis of weather effects on Covid-19 pandemic transmissions in select US counties".

[23] Altamimi A, Ahmed AE., "Climate factors and incidence of Middle East respiratory syndrome coronavirus," J Infect Public Health. 2020 May;13(5):704-708. doi: 10.1016/j.jiph.2019.11.011. Epub 2019 Dec 6. PMID: 31813836; PMCID: PMC7102558.

ENERGY EFFICIENCY AND INTERIOR COMFORT OF THE BUILDING WITH PASSIVE GEOTHERMAL HEATING IN TEMPERATE CLIMATE

Ismail Arroub[1*], Ahmed Bahlaoui[1], Soufiane Belhouideg[1]

[1,]*Team of Applied Physics and New Technologies (EPANT), Polydisciplinary Faculty, Sultan Moulay Slimane University, Beni Mellal, Morocco,ismail.arroub@gmail.com, 0000-0003-4263-2877, 0000-0003-2949-8618*

ABSTRACT

The objective of this work is to analyze the energetic efficiency of an individual building including an area of 109 m2 multi-zone, located in the region of Beni Mellal, Morocco, which is characterized by a very hot and dry climate in summer and a quite cold one in winter, by passive heating techniques. This study was performed using TRNSYS simulation software during the winter period of typical year. Our simulation consists in developing a comparative study with or without an earth-air heat exchanger (EAHX), in order to determine the best thermal performance. Our work aims to reduce the energy demand for heating and to improve the thermal comfort of the building by reducing the hours of under cooling. The results of the simulations show a significant potential for air heating. Indeed, for the coldest day of January (retained for this study), when the outside temperature is 2 °C, the heated temperature after using the EAHX in the studied area of the building is 11.5 °C. Moreover, the EAHX is an efficient system for building air heating in temperate climate like in Beni Mellal region.

Keywords: *Energy efficiency, building, earth-air heat exchanger, passive heating, TRNSYS*

1. INTRODUCTION

In recent years, the environmental concerns and limited convectional resources have led to identifying alternative sources of energy such as hydro, wind, magneto hydrodynamic (MHD), geothermal, ocean power, solar energy. Geothermal technologies can lead to important energy savings mainly related to heating and cooling in buildings. It is well known that the use of ground coupled heat exchanger leads to an efficient, economical, environmentally friendly design. For this reason, the use of geothermal systems has been extensively analyzed in the literature, especially for the improvement these systems can lead to heat and cool the buildings [1].

To supply comfortable Circumstances in the Buildings of sufficient ground space, a passive technology of cooling or heating, known as an EAHX can be utilized efficiently and effectively. It is also nominated earth tube heat exchanger, ground source heat pump, ground tube heat exchanger or Canadian well. The idea of utilizing ground thermal inertia for air conditioning is not a new method, but a modified concept that goes back to the last decades. The air used is oftentimes outside air for ventilation, but also rentable for totally or partially managing the construction thermal loads. The climatic conditions affect strongly the system performances.

The performances of EAHXs are evaluated numerically or experimentally [2,3], and in particular [4]. reports an analysis of data monitoring campaign on an EAHX system installed in a school building, in order to evaluate the influence of the EAHX system on soil temperature. However, Morshed et al. [5] developed two GAHE systems (one in dry soil and the other in wet soil using a dripping arrangement) and observed tha t the coefficient of performance of wet GAHE system is 20.9% higher than dry GAHE system. Similarly, Agrawal et al. [6,7], compared the performance of dry GAHE system and wet GAHE system and found that the performance of wet GAHE system is better than dry GAHE system in winter as well as in summer season.In the paper, the geothermal system for a residential user has been investigated through dynamic simulation performed using a model developed in TRNSYS software [8]. Therefore, we analyze the effect of integration the EAHX in a building for the coldest period (January 2020) in city of Beni Mella

2. METHODOLOGY

2.1. Weather data and location

The meteorological data used in this study were taken from a typical year weather file for the city of Beni Mellal, (32.36°N, -6.4°E). The atmospheric temperature is presented in figure 1, for the month of January of 2020. The ambient temperature of this month varies between 2.1 °C and 24.9 °C which are the lowest and highest temperatures observed during this period at 13th and 26th of January respectively. The large amplitude of the temperature perturbations is the characteristic of a hot temperate climate.
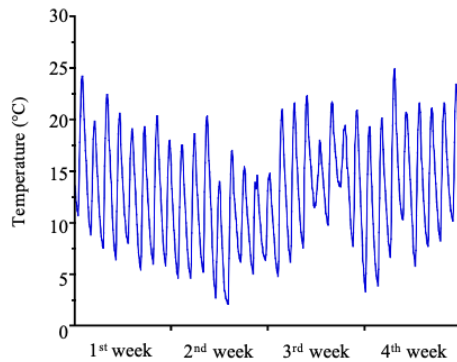
Figure 1. Ambient temperature (°C) for the period from 1st to 31th January.

2.2. Reference building

The studied building, is a detached villa type building, it is located in Beni Mellal and it is North-facing. Figure 2 present 2D architectural plans of the house which dimensions. Its floor area is of 109 m2 with a ceiling height of 2.8 m. The ground floor consists of four bedrooms, a living room, a bathroom, a hall and a balcony as shown in Figure 2.
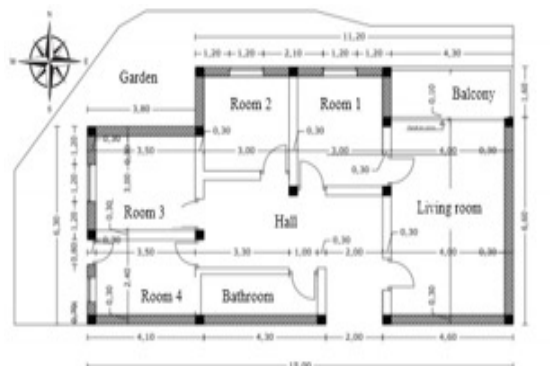
Figure 2. Building 2D plan

2.3. Dynamic simulation models

The dynamic thermal simulation was carried out through TRNSYS which designates Transient System Simulation software to simulate the building. The systems are simulated using components called "types" that are interconnected through time-dependent inputs and outputs. The building was simulated using Type 56 (TRNBuild) and connected to the soil using an Earth-Air Heat Exchanger (EAHX) Type 556 [15]. A time step of 1h was used to reduce computation time.

The building was Split into 7 thermal zones as it is presented in figure 3. Each room was specified as a thermal zone in order to find detailed information on each one of them. The study is made for room 1 and the simulation starts on 1st January and ends on 31th of the same month for the year of 2020.

For the computational study, the effect of the inclination pipe and its vertical parts is not considered into account since the horizontal part of the pipe is long enough. Thus, the EAHX is formed by only 1 pipe of PVC (polyvinyl chloride) with 35 m length. The pipe is assumed horizontal, and inhumed at the mean depth of 2.5 m. The thermo-physical characteristics of the PVC pipe, soil and air at average ambient temperature (20 °C) are reported in Table 1.

Table 1. Physical properties

	Thermal conductivity (W/m.K)	Specific heat (kJ/kg.K)	Density (kg/m^3)
Soil	1.4	1.3	1400
Air	0.025	1.01	1.16
PVC	0.17	1.3	1400

3. DISCUSSION

In this part, the essential results obtained by means of the dynamic thermal simulations carried out in this study are plotted and discussed in detail. The results concern the variations of the temperature with and without the EAHX in continuous operation over the period of the year 2020 (the month of January of 2020), as mentioned above. It should be noted that the results are presented for the room 1.

Figures 3 illustrate the temperature evolution for the month of January in the room 1, with and without integration of the EAHX. The air temperature

in the building has a minimum value surroundings 7 °C in the coldest day localized on January, but with the integration of the EAHX, this temperature undergoes an increase to 12°C. We note that the EAHX could be used also for the air precooling; for example, for the months of June and July, but this aspect is not treated since we are only interested in the building heating.

As a complement, figure 4 present the time evolution of the evaluated temperature, in the studied room, during a typical day of winter (the coldest day of the year) corresponding to January 13th of 2020. It is noted that the minimum / maximum temperature, in the studied room, is obtained for the 13th July and equal to 7.6 °C / 13.5 °C. This affects the thermal comfort zone caused by the lack of heating. The air temperatures obtained, in the room 1, after integration of EAHX is vary within the range of 11.5 °C – 14.8 °C; which gives a fairly significant difference of 3.9 °C between the temperature inside the studied room and that of the heat air (see figure 4).

Note that the ambient air temperature in the outside which occurs at 13th January is 2 °C, while the temperature of the air heated by the EAHX is 11.5 °C; which gives a fairly significant difference of 9.5 °C (see figure 1 and figure 4). Consequently, the above results show that the earth - air heat exchanger is a system more adapted to air heating in the buildings inside Beni Mellal city.
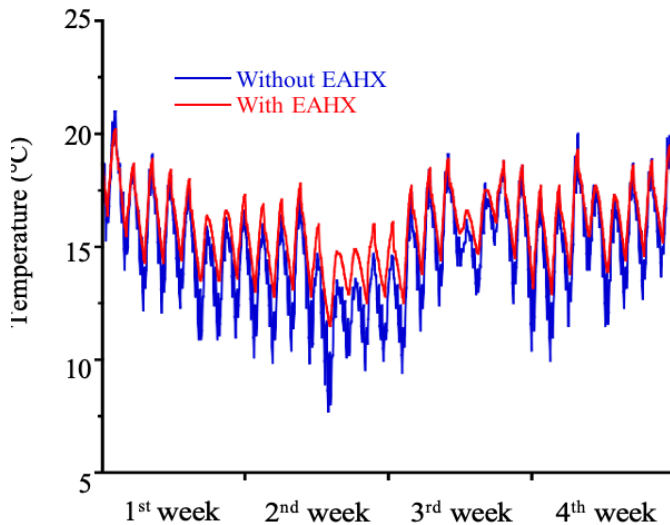
Figure 3. Temperature (°C) inside the room 1 for the period from 1st to 31th January
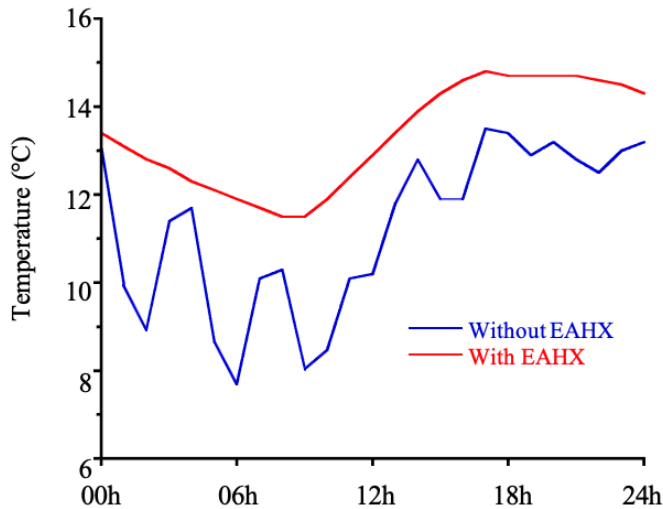
Figure 4. Temperature (°C) inside the room 1 for the coldest days of the year.

4. CONCLUSION

A numerical simulation of a case study of a house located in Beni Mellal (Morocco) was performed. The house was designed to be energy efficient by integrating a passive technique. A numerical model of the house has been developed in the frame of TRNSYS software. A parametric study was conducted to high-light the beneficial effect of Ground-coupled heating method by integration of an earth-air heat exchanger. The results show that the EAHX is an efficient system for building air heating in temperate climate like in Beni Mellal region. The ambient air temperature in the outside for the coldest day is 2 °C, while the temperature of the air heated by the EAHX is 11.5 °C; which gives a fairly significant difference of 9.5 °C.

REFERENCES

[1]   D'Agostino D., Mazzarella L., What is a nearly zero energy building? Overview, implementation and comparison of definitions. J. Build. Eng. 2019; 21; 200–212. https://doi.org/10.1016/j.jobe.2018.10.019.

[2]   Khabbaz, Mohamed, Benhamou, Brahim, Limam, Karim, Hollmuller, Pierre, Hamdi, Hassan, Bennouna, Amin, Experimental and numerical study of an earth-to-air heat exchanger for air cooling in a residential building in hot semi-arid climate. Energy Build. 2016; 125; 109-121, https://doi:10.1016/j.enbuild.2016. 04.071

[3]   Menhoudj, Sayeh, Mokhtari, Abderrahmane−Mejedoub, Benzaama, Mohamed-Hichem, Maalouf, Chadi, Lachi, Mohamed, Makhlouf, Mohammed, Study of the energy performance of an earth—air heat exchanger for refreshing buildings in Algeria. Energy Build. 2018; 158; 1602-1612, https://doi.org/10.1016/j.enbuild. 2017.11.056.

[4]   Grosso, Mario and Chiesa, Giacomo, Horizontal earth-to-air heat exchanger in Imola, Italy. A 30-Month- long monitoring campaign. Energy Procedia, 2015; 78; 73-78, https://. doi:10.1016/j.egypro.2015.11.117.

[5]   Morshed, W., Leso, L., Conti, L., Rossi, G., Simonini, S., Barbari, M., Cooling performance of earth-to-air heat exchangers applied to a poultry barn in semi-desert areas of South Iraq. Int. J. Agric. Biol. Eng. 2018; 11, 47-53, https://. doi: 10.25165/j.ijabe.20181103.3047.

[6]   Agrawal, K.K., Yadav, T., Misra, R., Agrawal, G. Das, Effect of soil moisture contents on thermal performance of earth-air-pipe heat exchanger for winter heating in arid climate: in situ measurement. Geothermics 2019; 77; 12-23, https://doi:10.1016/j.geothermics.2018.08.004.

[7]   Agrawal, K.K., Misra, R., Yadav, T., Agrawal, G.D., Jamuwa, D.K., Experimental study to investigate the effect of water impregnation on thermal performance of earth air tunnel heat exchanger for summer cooling in hot and arid climate. Renew. Energy, 2018; 120; 255-265, https://doi.org/10.1016/j.renene.2017.12.070.

[8]   Klein, S.A.; Beckman, W.A. TRNSYS 18: A Transient System Simulation Program; Solar Energy Laboratory, University of Wisconsin: Madison, WI, USA, 2017.

DETECTION OF RETINOPATHY DISEASES USING CONVOLUTIONAL NEURAL NETWORK BASED ON DISCRETE COSINE TRANSFORM

Mouad Kabbouri[1], Ali Okatan[1*]

[1]*Department of Software Engineering, Istanbul Aydin University, Istanbul, Turkey, aliokatan@aydin.edu.tr., 0000-0002-8893-9711*

ABSTRACT

This master thesis proposes a new approach to detecting retinopathy diseases using a convolutional neural network (CNN) based on discrete cosine transform (DCT). Retinopathy is a common eye disease that can cause vision loss if not diagnosed and treated early. The proposed method combines the power of CNN and DCT to improve the accuracy of detection. The input image is transformed into the frequency domain using DCT, which reduces the amount of noise and emphasizes the important features of the image. Then, the transformed image is fed into the CNN for classification. The performance of the proposed method is evaluated using a publicly available dataset of retinal images. The results show that the proposed method outperforms existing methods in terms of accuracy and computational efficiency. The proposed method has the potential to be used in real-world applications for early diagnosis and treatment of retinopathy diseases.

Keywords: *retinopathy diseases, convolutional neural network, discrete cosine transform, early diagnosis.*

1. INTRODUCTION

In this paper, we put forth an innovative approach for diagnosing retinopathy, a group of eye diseases causing significant damage to the retina, thus affecting vision. With an aim to enhance early detection techniques, our focus is on augmenting the accuracy, efficiency, and robustness of the diagnosis of retinopathy, a crucial step that can significantly improve patient outcomes. To this end, we present a unique model employing a Convolutional Neural Network (CNN), widely known for its proficiency in medical imaging tasks, integrated with the Discrete Cosine Transform (DCT), a potent technique in image processing.

This study uniquely merges the DCT into the CNN model, aspiring to provide superior feature extraction and representation. The DCT, by converting images from the spatial domain to the frequency domain, can help in the identification and extraction of essential features while concurrently reducing data dimensionality. The integration of DCT into the CNN model is anticipated to enhance the model's performance, leading to more precise and reliable diagnoses.

We employ the APTOS 2019 Blindness Detection dataset for this study, a substantial collection of fundus photographs captured under varied imaging conditions. This dataset serves as an excellent platform for developing and testing our model due to its complexity and diversity. Each image in the dataset has been evaluated by a clinician and classified on a severity scale: 0 - No Diabetic Retinopathy (DR), 1 - Mild DR, 2 - Moderate DR, 3 - Severe DR, and 4 - Proliferative DR as you see in the figure 1. The varying levels of disease severity within the dataset allow for rigorous testing and evaluation of our model.
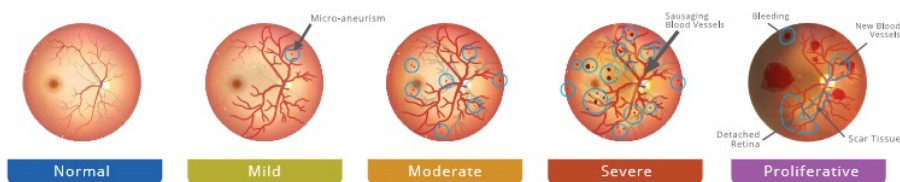

Figure 1. Stages of diabetic retinopathy

The main objective of our study is to develop a highly advanced, efficient, and reliable model for retinopathy detection, aiming to make substantial contributions to the early diagnosis and treatment of these diseases. By enhancing the capability of healthcare professionals to diagnose retinopathy in its early stages, we can significantly improve the prognosis for patients affected by these diseases, aiding in the prevention of vision loss.

In addition to this, our findings provide valuable insights into the application of CNNs and DCT in the domain of medical imaging. The proposed model's performance, evaluated using metrics such as accuracy, sensitivity, specificity, F1-score, and the area under the receiver operating characteristic (ROC) curve, will be juxtaposed with existing models and traditional diagnostic techniques. This comparison will pave the way for potential improvements and outline future research and development areas.

In conclusion, our research holds the potential to set new standards in retinopathy detection, with a novel CNN model integrated with DCT at its core. Our results are likely to significantly influence early detection, intervention, and treatment of retinopathy, thereby contributing to preserving vision for those affected by these diseases. Furthermore, the findings of this study could spearhead future research and innovation in medical imaging using deep learning techniques.

2. RELATED WORKS

Retinopathy detection has been one of the areas in medical diagnostics that have experienced considerable advancements due to the joint use of Convolutional Neural Networks (CNNs) and Discrete Cosine Transform (DCT). These two methodologies, when incorporated together, promise to enhance the accuracy, efficiency, and robustness of diagnostic algorithms.

According to Ali et al. [1], deep learning can significantly enhance the diagnosis accuracy and efficacy of treatment planning in medical imaging. Tools like Incremental Modular Networks (IMNets), which progressively add new modules instead of constructing a huge single network, can play a crucial role in this process. However, they should complement, not replace, the expertise of licensed healthcare professionals.

In a study involving Diabetic Retinopathy (DR) classification, a hybrid deep learning technique was proposed that utilized VGG16 and VGG19 convolutional neural networks [2]. The model classified images into four

severity groups with notable results. Gunasekaran et al. [3] emphasized the usefulness of retinopathy images in diagnosing diabetes, using a deep Recurrent Neural Network (RNN) to predict DR from fundus pictures, achieving an impressive 95.5% accuracy rate.

Khan et al. [4] developed several deep neural network architectures, including VGG-net, ResNet, and InceptionV3, which utilized transfer learning. The best accuracy in training and testing was achieved by InceptionV3 with rates of 81.2% and 79.4% respectively. Fang et al. [5] proposed a DAG network model for DR classification, extracting three key features from fundus images, resulting in reliable performance.

Elloumi et al. [6] proposed a novel method for screening smartphone-captured DR fundus images, using NasnetMobile for feature extraction. They reported high accuracy, precision, sensitivity, and specificity. Another research by Kanakaprabha et al. [7] compared various deep learning algorithms for predicting DR, including CNN, VGG16, VGG19, InceptionV2, ResNet50, MobileNetV2, and DenseNet.

Sridhar [8] suggested a CNN-based technique for DR detection using a public dataset from Kaggle, which greatly improved the detection accuracy. Das et al. [9] developed a DR classification system based on features of segmented fundus images, achieving a 97.2% precision rate and 98.7% accuracy.

In a study by Vives-Boix et al. [10], synaptic meta-plasticity significantly influenced the backpropagation of every convolutional layer in a model used to identify DR, producing excellent results. Luo et al. [11] suggested an automatic DR detection method using multi-view fundus images and CNN, with an attention mechanism for high performance.

After extracting textural characteristics with local binary patterns, Adriman [12] reported a performance assessment of DR systems utilizing several deep learning techniques. In order to increase the accessibility of the medical pictures, Fatima [13] suggested a complete approach based on a hybrid neural network for recognizing DR.

An Active Deep Learning Convolutional Neural Network (ADL-CNN) with a multi-layer architecture was created by Qureshi [15] for DR systems. Using the EyePACS dataset, the ADL-CNN model achieved an impressive

performance. Kalyani et al. [16] first used Deep learning reconstructed capsule networks to categorize DR, testing on the MESSIDOR dataset to obtain high accuracy.

Gayathri [17] utilized a multipath CNN and machine learning classifiers to develop an automatic DR detection system. Bodapati [18] built a composite DNN using a gated-attention mechanism for automatic DR severity classification.

Using adaptive machine learning, Math et al. [19] created a DR classification method that had remarkable sensitivity, specificity, and ROC curve area under the curve. Deep learning techniques were used by Gao [20] to provide a method for rating DR based on fundus fluorescein angiography. DR was diagnosed by Kobat et al. [21] using a pre-trained DenseNET model, with a cross-validation accuracy of 84.90%.

3. THE PROPOSED APPROACH

This paper introduces an efficient methodology for the detection of retinopathy diseases using Convolutional Neural Network (CNN) combined with Discrete Cosine Transform (DCT). The model is trained on the APTOS 2019 Blindness Detection dataset, which consists of thousands of retinal images collected from rural areas. This section presents an in-depth overview of the proposed approach, detailing the image preprocessing steps, Discrete Cosine Transform application, and the architecture of the developed CNN model.

Aptos 2019 blindness dataset which is a clinician rated each image for the severity of diabetic retinopathy on a scale from 0 to 4 where the numbers represent the extent of the complication as

Follows in table 1.

Table 1. Severity of diabetic retinopathy

SCALE	SEVERITY
0	No DR
1	Mild DR
2	Moderate DR
3	Severe DR
4	Proliferative DR

Image Preprocessing & DCT Application:

Before the actual preprocessing phase, a Discrete Cosine Transform (DCT) is applied to each image. DCT is a powerful tool used for image compression and reducing redundancies in image data, making it more manageable for the model. The process begins by converting the image to the YCrCb color space. The image is then split into its constituent channels, and a 2D DCT is applied to the Y channel. This is achieved using the get_image_dct() function:

```
def get_image_dct(image):
    # Convert to YCrCb
    ycbcr_img = cv2.cvtColor(image, cv2.COLOR_BGR2YCrCb)
    # Split the channels
    y, cb, cr = cv2.split(ycbcr_img)
    # Apply 2D Discrete Cosine Transform (DCT) to the Y channel
    dct_img = cv2.dct(np.float32(y)/255.0)
    return dct_img

    import cv2
    fig, ax = plt.subplots(1, 5, figsize=(15, 6))
    for i in range(5):
    sample = train_df[train_df['diagnosis'] == str(i)].sample(1)
    image_name = sample['id_code'].item()
    X = preprocess_image(cv2.imread(f"C:/Users/mouad/
    aptos2019-blindness-detection/train_images/{ image_name }"))
    ax[i].set_title(f"Image: { image_name }\n Label = {
    sample['diagnosis'].item() }",
    weight = 'bold', fontsize = 10)
    ax[i].axis('off')
    ax[i].imshow(X);
```

I've implemented a preprocessing phase as part of my machine learning pipeline. The goal of my project is to classify diabetic retinopathy images based on a specific diagnosis, which involves manipulating the images stored in a local directory. This involves using a Pandas DataFrame to manage the image metadata like filenames and corresponding diagnoses.

Here's a step-by-step explanation of my code:

1. I've written a function called get_image_dct. This function accepts an image and processes it as follows:

• I convert the color space of the image from BGR (Blue, Green, Red - a standard in OpenCV) to YCrCb (Luminance, Blue-difference Chroma, Red-difference Chroma). I used OpenCV's cv2.cvtColor function for this.

• Next, I separate the YCrCb image into its Y, Cr, and Cb components using the cv2.split function.

• I then apply a two-dimensional Discrete Cosine Transform (DCT) to the 'Y' component of the image using cv2.dct. Before the DCT, I normalize the 'Y' component by converting its datatype to float32 and scaling it to a 0-1 range.

• This function returns the DCT transformed 'Y' component.

2. The main part of the code is about visualizing some images. It creates a grid of subplots with a single row and five columns.

• For each unique diagnosis in the dataset, it selects a random image corresponding to that diagnosis.

• Each selected image is then read and preprocessed using the preprocess_image function.

• The preprocessed image is displayed in its respective subplot with the filename and corresponding diagnosis as the title. The axes are hidden for a cleaner look as you see in the figure 2 [23].
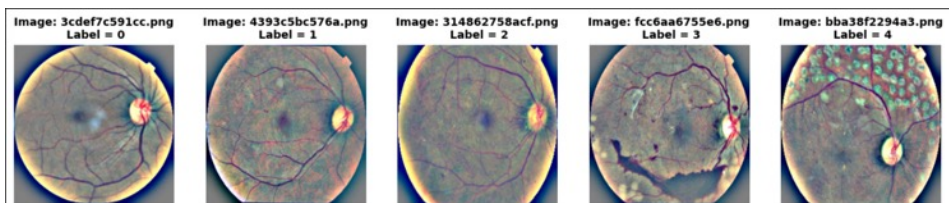

Figure 2. Preprocessed image

To sum it up, this preprocessing phase helps in preparing the images for further analysis and visualizing sample images from each class. This visualization aids in better understanding of the data and can provide insights into the kind of transformations needed for the images in order to improve the performance of the classification model. This application of DCT aids in emphasizing the features of the image that are critical for human perception, consequently enhancing the model's ability to recognize significant patterns.

3. MODEL ARCHITECTURE

A Sequential CNN model is used for the detection of retinopathy diseases. The model includes several convolutional layers for feature extraction, max pooling layers for spatial dimension reduction, dropout layers to minimize overfitting, and dense layers for final classification. The architecture of the model is detailed as follows:

model=Sequential()

model.add(Conv2D(filters=16,kernel size=2,padding="same",activation="relu",input_shape=(256,256,3)))

model.add(MaxPooling2D(pool_size=2))

model.add(Conv2D(filters=32,kernel_ size=2,padding="same",activation="relu"))

model.add(MaxPooling2D(pool_size=2))
model.add(Conv2D(filters=64,kernel_ size=2,padding="same",activation="relu"))

model.add(MaxPooling2D(pool_size=2))
model.add(Conv2D(filters=128,kernel_ size=2,padding="same",activation="relu"))

model.add(MaxPooling2D(pool_size=2))
model.add(Dropout(0.2))
model.add(Flatten())
model.add(Dense(512,activation="relu"))
model.add(Dropout(0.2))
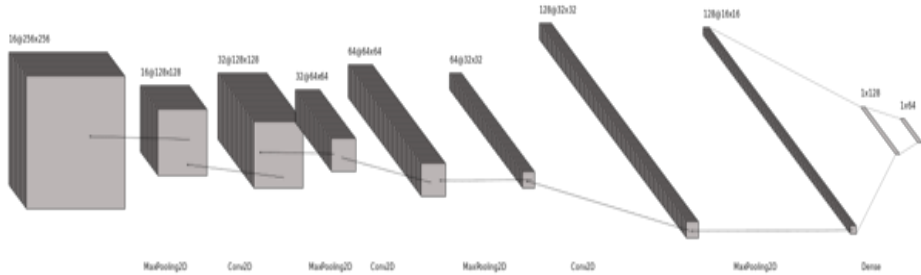*model.add(Dense(5,activation="softmax"))*

Figure 3. CNN model Architecture

During the preprocessing phase, the images underwent several transformations to ensure they are optimized for the model. The two functions, crop_image_from_gray() and preprocess_image(), are used to apply these transformations. The first function isolates the important regions of an image, while the second function converts the image to RGB, resizes it to the desired dimensions (224x224 in this case), and enhances the details by combining the original and blurred versions of the image.

This architecture begins with a 2D convolutional layer with 16 filters, a kernel size of 2, and 'ReLU' activation function. The input shape for this layer is 256x256x3, corresponding to the height, width, and number of channels in the input images. This layer is followed by a series of Conv2D and MaxPooling2D layers, gradually increasing the number of filters in the Conv2D layers from 16 to 128. These layers extract the critical features from the images and reduce their spatial dimensions, respectively.

Dropout layers are introduced to reduce overfitting, and a Flatten layer is used to flatten the features into a single dimension. Finally, two dense layers are used, where the last layer has five nodes corresponding to the five categories of diabetic retinopathy severity. The 'softmax' activation function in the final layer ensures the output values are probabilities that sum up to 1, with each probability indicating the likelihood of an image belonging to a particular class.
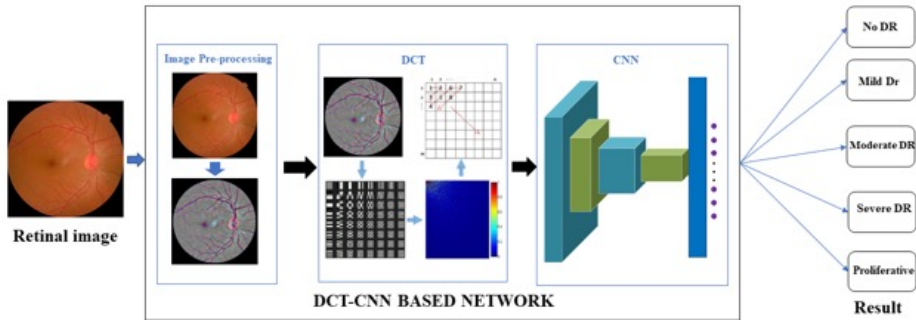
Figure 4. Block diagram of Detection of Retinopathy Diseases

The proposed methodology offers a promising approach for retinopathy detection by effectively combining image preprocessing, DCT application, and deep learning. The result is an efficient CNN-based model with enhanced ability to learn and detect various stages of retinopathy diseases from retinal images.

4. EXPERIMENTAL RESULTS

The model was trained and evaluated using a robust computational setup. The experiments were carried out on a 3.2 GHz machine with 16 GB of memory and a GTX 1650ti GPU. The development environment was Jupyter Notebook, provided by Anaconda, ensuring reliable, reproducible results.

4.1. Model Trained Using Our Developed Model

The developed model was trained and evaluated over 50 epochs. The model performance metrics, including loss (cross-entropy loss) and accuracy, were observed for both the training and validation set for each epoch.

The initial epoch revealed a training accuracy of 66.05%. On the validation set, the accuracy was 70.31%. This established the baseline performance of our model.

As the epochs progressed, we noticed an increase in accuracy and a decrease in loss on both the training and validation sets, indicating the learning capability of our model. By the end of the second epoch, the model achieved a training accuracy of 72.43%, and the validation accuracy improved to 70.74%.

By the 7th epoch, the validation accuracy had reached 72.44%, and the model's loss had reduced to 0.494. At the 8th epoch, we observed a significant jump in the validation accuracy, reaching 74.72%. This suggested that the model was generalizing well and was capable of classifying unseen data accurately.

However, in the following epochs, there was a slight increase in the validation loss, despite the model's improved accuracy, suggesting a bit of overfitting. After the 10th epoch, the training accuracy reached 83.78%, and the validation accuracy stood at 78.01%.

4.2. Model Trained Using Pretrained Model Xception
In my research project, I leveraged the power of the pre-trained Xception model for an image classification task. After applying my preprocessing pipeline and running the model, the Xception model demonstrated strong performance. Specifically, during the 21st epoch, the Xception model achieved an impressive accuracy of 74.52% on the validation set. This result underscores the efficacy of the Xception model in this particular image classification task, illustrating its robust generalization capabilities.

4.3. Model Trained Using Pretrained Model Resnet152v2
In a parallel analysis during my research, I applied the same image preprocessing procedure to another renowned pre-trained model, ResNet152V2, in the same image classification task. The performance of the ResNet152V2 model was robust and achieved a notable accuracy. Precisely, during the evaluation stage, the ResNet152V2 model reached an accuracy of 73.07% on the validation set. This result highlights the strong performance and the model's capability to effectively generalize in this specific image classification context.

In conclusion, our developed model demonstrated promising performance with accuracy of 78%, achieving a respectable accuracy in classifying the severity of retinopathy in the APTOS 2019 Blindness Detection dataset. Future work may include tuning the model to mitigate overfitting, enhancing its generalizability, and potentially improving the model's performance further.

5. CONCLUSION
One of the illnesses with the fastest recent growth rates is diabetes. A patient with diabetes has a 30% chance of developing diabetic retinopathy,

according to several surveys. There are several phases of DR, from moderate to severe, and PDR (Proliferative Diabetic Retinopathy) is the last stage. If the condition is not discovered in the earlier stages, it progresses to blindness, floaters, and impaired vision in its later stages. There is still a need for simple access to such models despite the fact that several computer vision-based strategies for the automatic identification of DR employing hands-on engineering and end-to-end learning approaches have been offered.

In this regard, the study described in this paper suggests a novel method for early DR detection based on a Convolutional Neural Network (CNN) model based on Discrete Cosine Transform (DCT) that is specially designed for mobile devices.

In developing this model, we utilized one publicly accessible Kaggle dataset for training and validating our CNN-based DCT network. We found that image pre-processing is an essential step in this process.

Our results indicate that the CNN-based DCT model successfully classifies the early stages of DR. This aligns with our central aim of encouraging early detection before the progression to more advanced stages such as PDR. However, it's important to note that the model does encounter some difficulty in classifying the final stages of DR.

Early DR stages are notoriously difficult to classify, as confirmed by related work in the field. However, our proposed CNN-based DCT model exhibits encouraging results for early stage classification. It particularly excels at distinguishing Non_DR from the mild to moderate stages, thanks to the pre-processing technique employed.

Nonetheless, our study did uncover a limitation in the model's performance when it came to classifying the last two stages of the disease. We believe this could be due to the fact that the characteristic features of DR's later stages do not replace the earlier stages' features but rather augment them. This means that features from the earlier stages still exist in the later stages, complicating their differentiation. Future work will aim to improve the model's performance for these advanced stages.

REFERENCES

[1.] Ali, R.; Hardie, R.C.; Narayanan, B.N.; Kebede, T.M. IMNets: Deep Learning Using an Incremental Modular Network Synthesis Approach for Medical Imaging Applications. *Appl. Sci.* **2022**, *12*, 5500. [**Google Scholar**] [**CrossRef**]

[2.] Menaouer, B.; Dermane, Z.; El Houda Kebir, N.; Matta, N. Diabetic Retinopathy Classification Using Hybrid Deep Learning Approach. *SN Comput. Sci.* **2022**, *3*, 357. [**Google Scholar**] [**CrossRef**]

[3.] Gunasekaran, K.; Pitchai, R.; Chaitanya, G.K.; Selvaraj, D.; Annie Sheryl, S.; Almoallim, H.S.; Alharbi, S.A.; Raghavan, S.S.; Tesemma, B.G. A Deep Learning Framework for Earlier Prediction of Diabetic Retinopathy from Fundus Photographs. *Biomed Res. Int.* **2022**, *2022*, 1–15. [**Google Scholar**] [**CrossRef**]

[4.] Khan, A.; Kulkarni, N.; Kumar, A.; Kamat, A. D-CNN and Image Processing Based Approach for Diabetic Retinopathy Classification. *Appl. Inf. Process. Syst.* **2022**, *1354*, 283–291. [**Google Scholar**] [**CrossRef**]

[5.] Fang, L.; Qiao, H. Diabetic Retinopathy Classification Using a Novel DAG Network Based on Multi-Feature of Fundus Images. *Biomed. Signal Process. Control* **2022**, *77*, 103810. [**Google Scholar**] [**CrossRef**]

[6.] Elloumi, Y.; Abroug, N.; Bedoui, M.H. End-to-End Mobile System for Diabetic Retinopathy Screening Based on Lightweight Deep Neural Network. *Lect. Notes Comput. Sci. (Incl. Subser. Lect. Notes Artif. Intell. Lect. Notes Bioinform.)* **2022**, *13205 LNCS*, 66–77. [**Google Scholar**] [**CrossRef**]

[7.] Kanakaprabha, S.; Radha, D.; Santhanalakshmi, S. Diabetic Retinopathy Detection Using Deep Learning Models. *Int.* **2022**, *302*, 75–90. [**Google Scholar**] [**CrossRef**]

[8.] Sridhar, S.; PradeepKandhasamy, J.; Sinthuja, M.; Sterlin Minish, T.N. Diabetic Retinopathy Detection Using Convolutional Nueral Networks Algorithm. *Mater. Today Proc.* **2021**. [**Google Scholar**] [**CrossRef**]

[9.] Das, S.; Kharbanda, K.; Suchetha, M.; Raman, R.; Dhas, E. Deep Learning Architecture Based on Segmented Fundus Image Features

for Classification of Diabetic Retinopathy. *Biomed. Signal Process. Control* **2021**, *68*, 102600. [**Google Scholar**] [**CrossRef**]

[10.]Vives-Boix, V.; Ruiz-Fernández, D. Diabetic Retinopathy Detection through Convolutional Neural Networks with Synaptic Metaplasticity. *Comput. Methods Programs Biomed.* **2021**, *206*, 106094. [**Google Scholar**] [**CrossRef**]

[11.]Luo, X.; Pu, Z.; Xu, Y.; Wong, W.K.; Su, J.; Dou, X.; Ye, B.; Hu, J.; Mou, L. MVDRNet: Multi-View Diabetic Retinopathy Detection by Combining DCNNs and Attention Mechanisms. *Pattern Recognit.* **2021**, *120*, 108104. [**Google Scholar**] [**CrossRef**]

[12.]Adriman, R.; Muchtar, K.; Maulina, N. Performance Evaluation of Binary Classification of Diabetic Retinopathy through Deep Learning Techniques Using Texture Feature. *Procedia Comput. Sci.* **2021**, *179*, 88–94. [**Google Scholar**] [**CrossRef**]

[13.]Fatima; Imran, M.; Ullah, A.; Arif, M.; Noor, R. A Unified Technique for Entropy Enhancement Based Diabetic Retinopathy Detection Using Hybrid Neural Network. *Comput. Biol. Med.* **2022**, *145*, 105424. [**Google Scholar**] [**CrossRef**]

[14.]Ragab, M.; Aljedaibi, W.H.; Nahhas, A.F.; Alzahrani, I.R. Computer Aided Diagnosis of Diabetic Retinopathy Grading Using Spiking Neural Network. *Comput. Electr. Eng.* **2022**, *101*, 108014. [**Google Scholar**] [**CrossRef**]

[15.]Qureshi, I.; Ma, J.; Abbas, Q. Diabetic retinopathy detection and stage classification in eye fundus images using active deep learning. *Multimed Tools Appl* **2021**, *80*, 11691–11721. [**Google Scholar**] [**CrossRef**]

[16.]Kalyani, G.; Janakiramaiah, B.; Karuna, A.; Prasad, L.V. Narasimha Diabetic Retinopathy Detection and Classification Using Capsule Networks. *Complex Intell. Syst.* **2021**, *2021*, 1–14. [**Google Scholar**] [**CrossRef**]

[17.]Gayathri, S.; Gopi, V.P.; Palanisamy, P. Diabetic Retinopathy Classification Based on Multipath CNN and Machine Learning Classifiers. *Phys. Eng. Sci. Med.* **2021**, *44*, 639–653. [**Google Scholar**] [**CrossRef**] [**PubMed**]

[18.]Bodapati, J.D.; Shaik, N.S.; Naralasetti, V. Composite Deep Neural

Network with Gated-Attention Mechanism for Diabetic Retinopathy Severity Classification. *J. Ambient Intell. Humaniz. Comput.* **2021**, *12*, 9825–9839. [**Google Scholar**] [**CrossRef**]

[19.] Math, L.; Fatima, R. Adaptive Machine Learning Classification for Diabetic Retinopathy. *Multimed. Tools Appl.* **2021**, *80*, 5173–5186. [**Google Scholar**] [**CrossRef**]

[20.] Gao, Z.; Jin, K.; Yan, Y.; Liu, X.; Shi, Y.; Ge, Y.; Pan, X.; Lu, Y.; Wu, J.; Wang, Y.; et al. End-to-End Diabetic Retinopathy Grading Based on Fundus Fluorescein Angiography Images Using Deep Learning. *Graefe's Arch. Clin. Exp. Ophthalmol.* **2022**, *260*, 1663–1673. [**Google Scholar**] [**CrossRef**] [**PubMed**]

[21.] Kobat, S.G.; Baygin, N.; Yusufoglu, E.; Baygin, M.; Barua, P.D.; Dogan, S.; Yaman, O.; Celiker, U.; Yildirim, H.; Tan, R.S.; et al. Automated Diabetic Retinopathy Detection Using Horizontal and Vertical Patch Division-Based Pre-Trained DenseNET with Digital Fundus Images. *Diagnostics* **2022**, *12*, 1975. [**Google Scholar**] [**CrossRef**]

[22.] Dr. OKATAN Ali, Karlık B, Demirezen F, Detection of retinopathy diseases using an artificial neural network based on the discrete cosine transform January 2009 Neural Network World 19(2):215-221

[23.] Diabetic Retinopathy (resized), Resized version of the Diabetic Retinopathy Kaggle competition dataset https://www.kaggle.com/ tanlikesmath/diabetic-retinopathy-resized,2019

[24.] Diabetic Retinopathy Detection SHAP, Data Preprocessing https:// www.kaggle.com/code/simrahikram/diabetic-retinopathy-detection-shap/notebook

[25.] K. Simonyan and A. Zisserman. Very deep convolutional networks for large-scale image recognition. arXiv preprintarXiv:1409.1556, 2014.

[26.] Tajbakhsh N, Shin JY, Gurudu SR, Hurst RT, Kendall CB, Gotway MB, et al. Convolutional neural networks for medical image analysis: full training or fine tuning? IEEE Trans Med Imaging. 2016;35(5):1299–312.

DESIGN OF MICROSCOPE ILLUMINATION SYSTEM BASED ON LED LIGHT SOURCE AND COLLIMATOR USING ZEMAX SOFTWARE

Ismahen Osmani [1*], Fouad Lakhdari [1],
Mohamed Loghrab [1], Mounir Bouchaour [1]

*[1]Unit of Research in Optics and Photonic (UROP),
Centre for the Development of advanced Technologies (CDTA),
Algeria, iosmani@cdta.dz, 0009-0002-3194-2124*

ABSTRACT

In this work, we study how to achieve a high quality lighting system construction capable of efficiently collects and focus the light emitted from an extended source in order to completely and homogeneously fill the condenser aperture diaphragm with axial and parallel light. The Zemax® optics simulation software is utilized to design a collimating optical system for the LED light source using the Non-Sequential Components. The simulation of the collimated light source is obtained of various parameters: the optical efficiency, light power and irradiance.

Keywords: *Illumination of microscope, LED, collimator, Zemax® optical design software*

1. INTRODUCTION

Illumination of the optical microscope is a very important parameter which must be fulfilled in order to obtain optimum performance. There are different light sources available for lighting microscopes, both for surveys and routine observation. In general, microscope illumination systems are optimized to produce the maximum light intensity, from a relatively small source, such as incandescent lamp filament, Arc lamps, lasers or the surface area of light - emitting diodes (LEDs) for two illuminating systems: critical illuminating system and Kohler illuminating. The illumination and orientation of light rays through the optical microscope can be controlled with lenses, diaphragms, prisms and other optical components strategically placed to achieve the desired degree [1,2] .

Among the most promising of emerging technologies for illumination systems in optical microscopy is the light- emitting diode (LED). LED-based illumination sources targeted at microscopy utilize three optical collimators to reflect and collimate the light generated inside the semiconductor die [3, 4]. In this study, a collimation optical system for LED source is presented. The design of collimating optical system for the LED light source by Zemax® optics simulation software is carried. The behavior of some parameters that characterize the performance of the optical system is assessed.

2. THEORY

The objective of this study is to design a free-form lens (collimator) for LEDs to be used as an optical microscope illumination system, in which highly collimated light is required.
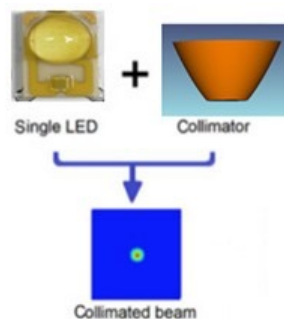

Figure 1. The principle of proposed uniform LED illumination system.

The present work used a Rebel LED Cool White, for illustration purposes. As shown in Table 1, the main features of the Rebel LED include a wavelength Range of 4500K to 10000K (Cool White),an optical power of 700mW, and a radiation angle of 120°. Figure 2. Shows the mechanical dimension of the led.

Table 1. Main features of Rebel LED

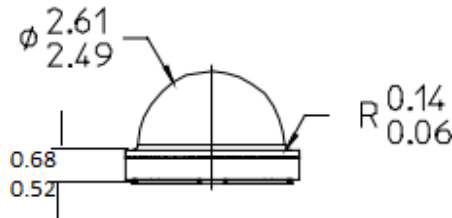| Parameter	Cool-White
LED color	Cool-White
Typical Lumens	180lm
Typical Wavelength	6500K
Wavelength Range	4500K to 10000K
Beam Angle	120°
Typical Forward Voltage	3Vf
Maximum Forward Voltage	3.99Vf

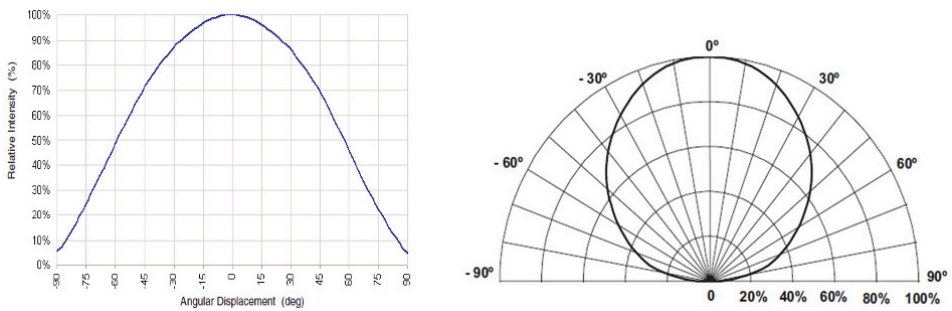**Figure 2**. Mechanical dimension of the led.

Figure 3.Typical representative spatial and polar radiation pattern for cool-white lambertian

3. RESULTS AND DISCUSSION

The Zemax® optics simulation software is utilized to design a collimating optical system for the LED light source using the Non-Sequential Components. The collimator designed in this study is manufactured in PMMA which is a poly(methyl methacrylate) material with an optical refraction index of 1.51 at 365 nm [5]. Figure 4 (a) and

(b) illustrate the calculated Fresnel optical transmittance of the chosen material at the air/PMMA and PMMA/air interfaces, respectively, as a function of the incident angle. The total reflection angle at the PMMA / air interface is approximately 41°.
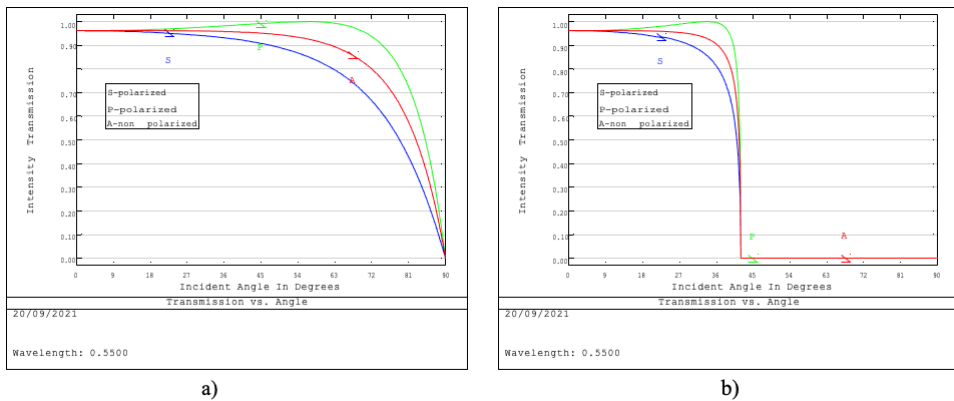

a)   b)

Figure 4. Optical transmission coefficients as function of incident angle for: a) Air to poly PMMA interface, and b)PMMA to air interface.

The collimator is imported in the software and simulations are performed for the radial source to check the performance of the freeform lens. Parameters selected for the simulation are listed in Table 2.

Table 2. Parameters selected for the simulation

Parameter	Description
Source type	Rebel LED
Radiation pattern	Lambertian
Collimator diameter	20 mm
Collimator length	10 mm
Material	PMMA
Number of LEDs	1
Tracing ray	1.000.000

Figure 5 shows the ray tracing through the whole system. In this design, we set the power is 3 watt. All light rays can be transferred to parallel rays after the collimating optical system, which results in a circular shape beam. The beam diameter coinciding with the diameter of the reflector. Since the LED is a Lambertian light source, the beam energy is focused in the center of the circular beam.
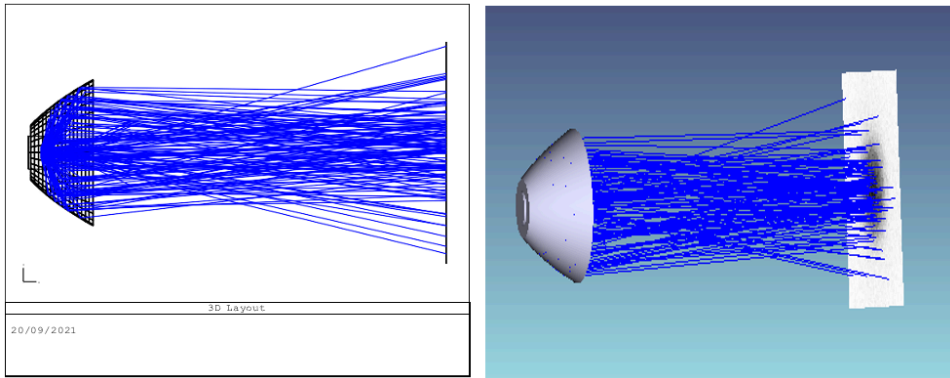

Figure 5. Ray trace layout of collimator lens with LED

With ray file consisting of 1 million rays is placed 80 mm away from the lens, Fig. 6 shows spot size and incoherent irradiance distribution obtained at the detector. Simulation results indicated that the light intensity distribution concentrate in the centre. According to this result, we can obtain through the whole collimating optical system uniform illumination.
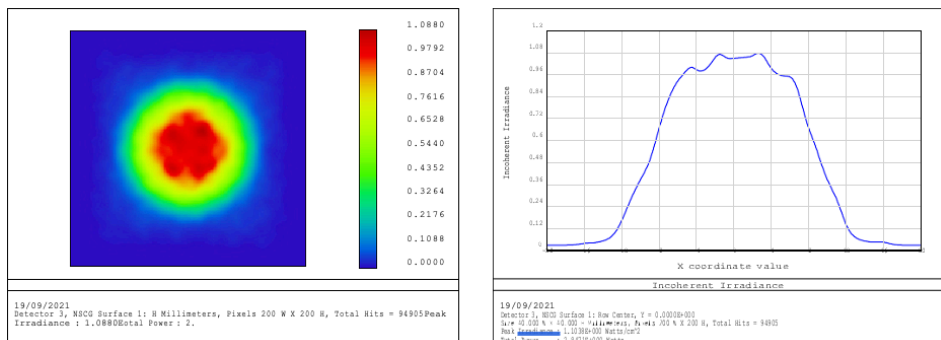

Figure 6. incoherent irradiance distribution from a radial source with Lambertian pattern when combined with a freeform lens

For characterized the quality of the beam that emerges from the optical system, two parameters must becalculated [6]:

-The optical efficiency, defined as the ratio of the luminous flux emitted by LED and the collected luminous flux is obtained by:

$$\text{optical efficiency} = F_C/FL \qquad (1)$$

Where FL and Fc , are respectively, the luminous flux emitted by LED and the collected luminous flux.

-The uniformity of the beam after passing through the system is obtained by:

$$Uniformity = \frac{Eave}{Emax} \qquad (2)$$

Where E ave and E max , the maximum and average values of the irradiance along the flat area of the beam. After the calculation, the optical efficiency of the overall optical system is approximately 80.3%. Then, the uniformity of rays that travel through the lens system to the detector is 14%

4. CONCLUSION

This paper presented a freeform lens for collimating light emitted from a LED.The optical performance of the proposed freeform lens (PMMA) was simulated by ZEMAX® for a LED (Cool White) with a power 3 W and a full radiation angle of 120°. The parameters which characterize the quality of the beam exiting the optical system were calculated by a virtual detector (40x40mm) positioned behind the optical system at 80 mm.

REFERENCES

[1] B. Herman and J. J. Lemasters (eds.), Optical Microscopy: Emerging Methods and Applications. Academic Press, New York, 1993, pp 441.

[2] S. Bradbury and B. Bracegirdle, Introduction to Light Microscopy. BIOS Scientific Publishers Ltd., Oxford,UK, 1998, pp 123..

[3] I. Inoué, S. and K.R. Spring. Video Microscopy: The Fundamentals, Plenum Press, New York, 1197, pp 49-58

[4] Horniak (Ed.), Encyclopedia of Imaging Science and Technology, vol. 2. John Wiley and Sons, New York, 2002, pp 1106-1141.

[5] PLEXIGLAS®8012 Material Manual, (Evonik Performance Materials GmbH, Essen, Germany).

[6] Kudaev S. and Schreiber P., "Automated optimization of non-imaging for luminaires", Proc. SPIE 5942, 232- 238(2005).

COMPUTATIONAL MODELING OF COLD FLOW CHARACTERISTICS OF A SINGLE CYLINDER INTERNAL COMBUSTION ENGINE FOR DIFFERENT TURBULENCE MODELS

İsmail Hakkı Savcı[1], M. Zafer Gül[2]

[1] Department of CAE, Ford Otosan, Istanbul, Turkey
[2] Department of Mechanical Engineering, Marmara University, Istanbul, Turkey
isavci@ford.com.tr,zgul@marmara.edu.tr, 0000-0002-5943-7763

ABSTRACT

The recent developments of the CFD tools enable predicting the fluid dynamic, heat transfer, combustion, chemical reaction and spray formation process even in very complex geometries with a sufficient degree of accuracy and acceptable computational costs by numerical solutions of the governing conservation equations that have become a realizable goal. The principal components of these multidimensional engine flow models contain the mathematical models, the discretization procedures, and the solution algorithm. In addition, mathematical models or equations are used to describe the flow processes. Especially turbulence model, describing the small-scale features of the flow, is essential. The dynamic mesh model in Star-CD can be used to model flows where the shape of the domain changes with time due to motion on the domain boundaries. The update of the volume mesh is handled automatically by Star-CD at each time step based on the new positions of the boundaries. To use the dynamic mesh model, you need to provide a starting volume mesh and describe the motion as valve profile of any moving zones in the model. A simplified 3D geometry (from Imperial College compressing engine) will be used for this work, consisting of a simple compressor geometry, the bottom wall representing the piston. The simulation will be performed in an axisymmetric geometry from the TDC position (i.e., CA =0 0) to the end of the compression stroke (i.e., CA=3600). The development of CFD methodology for IC engine design represents a particular challenge due to the complex physics and mechanics. Turbulence modeling is one of the critical parameters for ICE CFD applications. Standard k-□ model has been widely used for the CFD calculation for the IC engine applications, other turbulence models are used as k-□-□ model (Gul extended a three-equation model) that can have a better account for compression and expansion effects. The main task of this project is to provide a numerical simulation of the intake flow field

and axis-symmetric cylinder. Two- dimensional computational analyses were performed on the axis-symmetric cylinder with k-□-□ and k-□ turbulence model. Results of the two-dimensional analysis were compared the numerical results to the flow field measurement.

Keywords: *ICE, CFD, Turbulence, cylinder*

1. INTRODUCTION

Multi-dimensional CFD analysis is important especially in the case of simulation of the cylinder since the design in unconventional. Multi-dimensional analysis can provide valuable information in comparing the flow fields of the axisymmetry [1]. Two-dimensional computational fluid dynamic analysis was performed on the axissymetry valve engine using STAR-CD [2]. Modern commercial CFD tools like STAR-CD offer more complex tools like turbulence modeling, dynamic mesh modification etc. which could be utilized for simulation. Also visualization tools as En-sight and STAR-CD can be used to plot and understand the flow features more effectively [3-5].

Two-dimensional analysis allows us to model the system in more detail without having the computational cost and effort of a three-dimensional analysis. It is important to capture the 2D effects of flow through the valve in order to study the local effects such as recirculation, swirl etc. [6-9].

In this study, two sets of simulations were performed for part load at 200 RPM with different compression ratios 3.5, 6.7 respectively with same valve profile. Multi-dimensional engine modeling method was built and developed to calculate of fluid flow in an idealized version of axisymmetric engine. Turbulent flow in-cylinder was considered. For the fluid flow, standard k-ε turbulence model and RNG k-ε turbulence model are utilized. Several cycles were run and convergence was monitored based on the mass balance inside the cylinder.

The in-cylinder flow in axisymmetric geometries and the flow through the inlet valve for unsteady conditions are investigated and experimental results are presented. The governing equations subject to relevant boundary conditions were solved numerically using finite-volume method. The upwind technique was employed to discretize the convective terms. PISO algorithm was used.
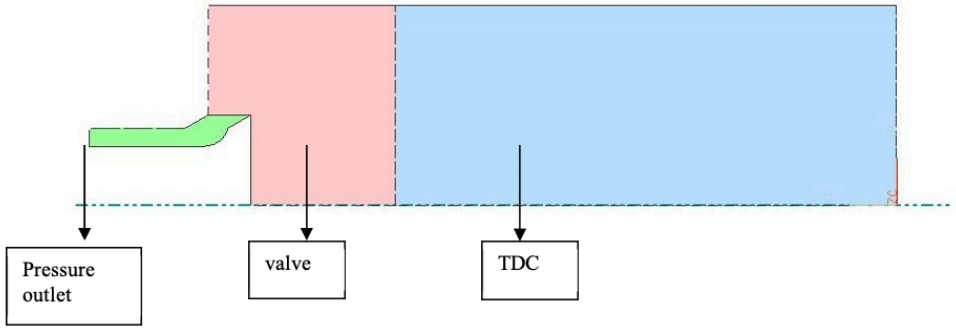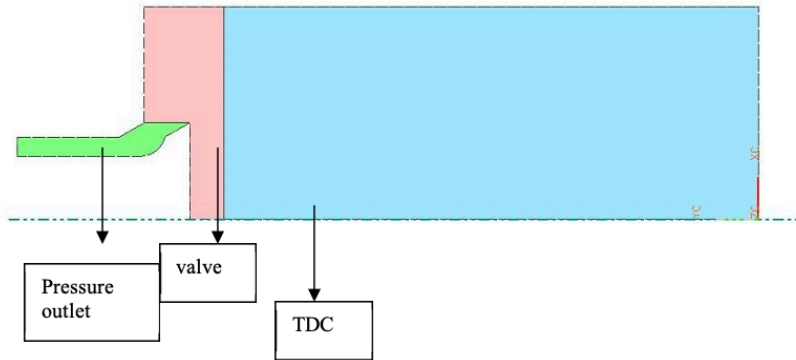
Figure 1. Geometry of the Case I

Figure 2. Geometry of the Case II

2. COMPUTATIONAL MODELLING

The computer code STARCD was used to model the intake system in axisymmetry engine. The configuration of the cylinder with its ports is shown in Fig. 3.The engine parameters used in this study are listed in Table 1. The engine had a bore of 75 mm and a stroke of 94 mm.

The cylinder is axisymmetric and exhaust valves are located at the cylinder axis. In order to obtain flow field and combustion characteristics, the ensemble-averaged differential form of continuity, momentum, enthalpy and standard k-ε equations are solved with appropriate boundary conditions [10-12].
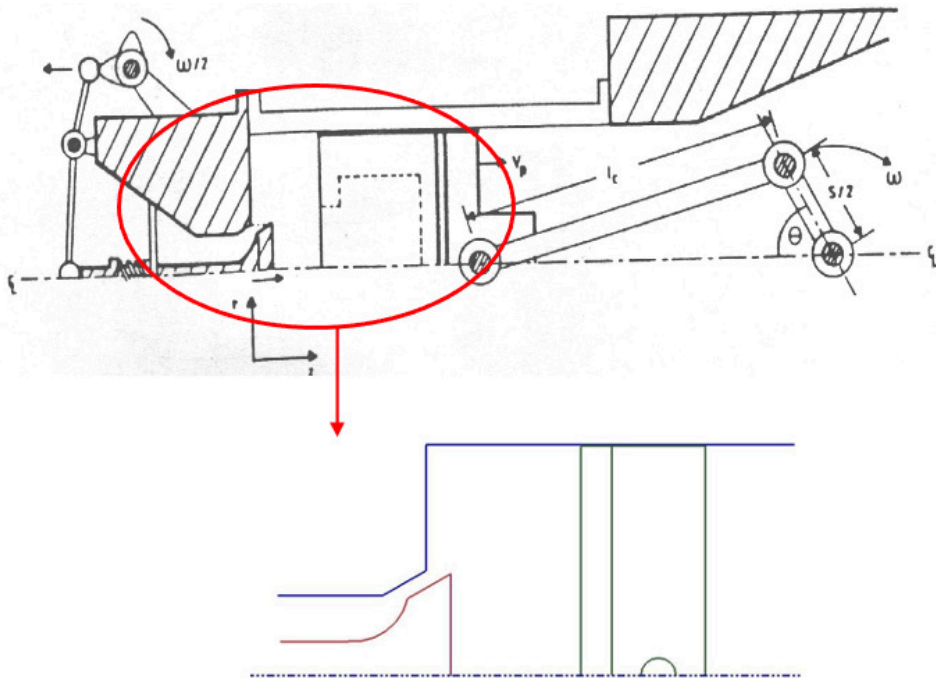
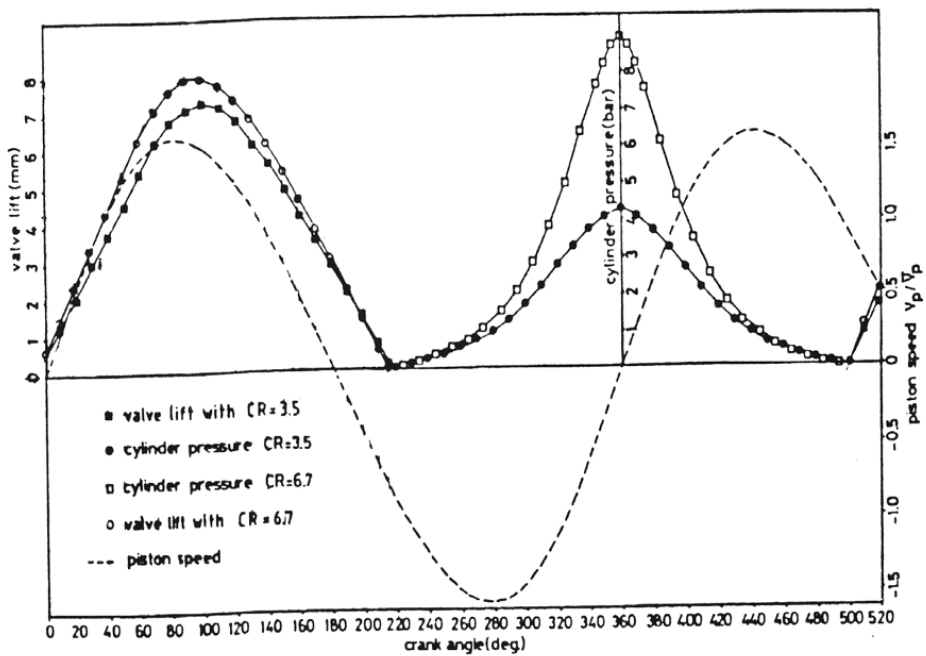**Figure 3.** Diagram of Imperial College Compressing Engine Simulator

Figure 4. Variation of Valve Lift, Piston Speed and Cylinder Pressure with Crank Angle of the Model Engines

The simulations were performed through the intake and compression strokes only. The exhaust system in this engine was not modeled since the exhaust valves were not considered to open. Details of the computational mesh are shown in Figure . The mesh had about 380,000 cells. Pressure inflow boundaries were imposed at the open ends of the intake runners. The calculations were started at a crank angle of 345 degrees (15 degrees before TDC the beginning of the intake stroke). The air, in the cylinder was considered to be quiescent at the beginning of the simulation.

Table 1. Details of Test Cases; the Imperial College 2D Engine Simulator

	Case I	**Case II**
Cylinder Bore (mm)	75	75
Stroke (mm)	94	94
Connecting-Rod Length (mm)	363.5	363.5
Compression Ratio	3.5	6.7
Engine Speed (rpm)	200	200
Mean Piston Velocity (m/s)	0.626667	0.626667
Max. Valve Lift (L_{max}) (mm)	7.3	8
Valve Diameter (D_v) (mm)	34	34
L_{max}/D_v	0.21	0.24
Valve seat angle	60º	60º

Two different cases are simulated. Table 1 lists these cases with a description of each cases.

At the beginning of the computation the inlet and initial values of variables, including mass flow rate, radial and axial velocity components, must be specified. The computation started at TDC and the initial velocity assumed as zero. However, to decrease the uncertainties the results were evaluated after one complete cycle run (i.e. after 360o). Details of operating conditions are in the Table 2.

Table 2. Valve Opening and Closing and Estimated Temperatures of the Engine Simulator

	Case I	**Case II**
Valve opening for intake	-6° CA	-6° CA
Valve closing for intake	226° CA	226° CA
Valve opening for exhaust	496° CA	496° CA
Valve closing for intake	6° CA	6° CA
Cylinder Wall Temp (K)	340	350
Cylinder Head & Wall (K	340	350
Piston (K)	360	370

Star-CD uses PISO algorithm for transient flow solution. The simulation was run over 360 time steps of 0.5 ca each, hence covering the opens cycle. This time step led to average Courant numbers within the mesh being in range 0.1 to 1. Typical runs took 2 days on HP-Unix machine. Post Processing information being written out for pressure, three components of velocity, turbulence intensity and density.
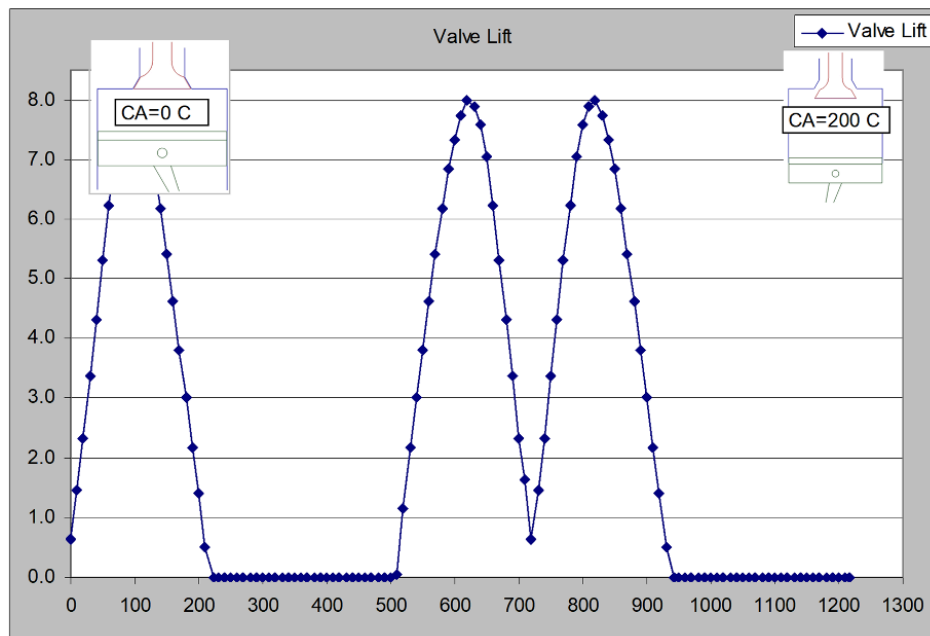

Figure 5. Valve Lift of the Engine Simulator

The simulations was commenced at 900C TDC. The cylinder was initiated to have zero velocity with a pressure and temperature of 109.3 kPa and 299 K respectively.

The cylinder pressure, species densities, turbulent kinetic energy and turbulence length scale are assumed to be uniform at the beginning of computation at the intake valve closure. The turbulent kinetic energy and dissipation rate within the cylinder and ducts were initialized at 1 m2/s2 and 1000 m2/s3 respectively, representing a relatively quiescent fluid with turbulent viscosity of close to 10-4 kg/s/m.

When the numerical solutions obtained on different grids agree to within a level of tolerance specified by the user, they are referred to as "grid converged" solutions. The concept of grid convergence applies to the finite-volume approach also where numerical solution, if correct, becomes independent of the grid as the cell reduced. It is very important that you investigate the effect of grid resolution on the solution in every CFD problem you solve. A CFD solution cannot be trusted unless you have convinced yourself that the solution is grid converged to an acceptance level of tolerance (which would be problem dependent) [13-15].

In order to obtain a solution independent of the grid distribution, grid sensitivity tests can be performed by tracing the cylinder pressure against crank angle. It is found that the solution becomes almost independent with uniform 250 grids in ξ direction and 150 uniform grids in the r-direction.

3. RESULTS AND DISCUSSION

In this study turbulent flow in an idealized homogeneous axissymetric engine are analyzed numerically. The valve is modeled so valve effects are taken into account. Computations are performed for different compression ratio r=3.7, r=6 respectively, with constant engine speed N=200 rpm, stroke L=0.09 m and ri= 0.04 m and rd=0.0567 m are chosen. Ideal gas is used to model compressible effects as a air.

For both test cases an overall impression of the in-cylinder behavior is provided in terms of plots at selected crank angles. All data shown in figures were obtained for 300000 grid-density run. The predictions of the standard k-e and RNG turbulence model was presented in figures. Computational grid arrangements for test Case I and Case II can be seen in the Figure 6.
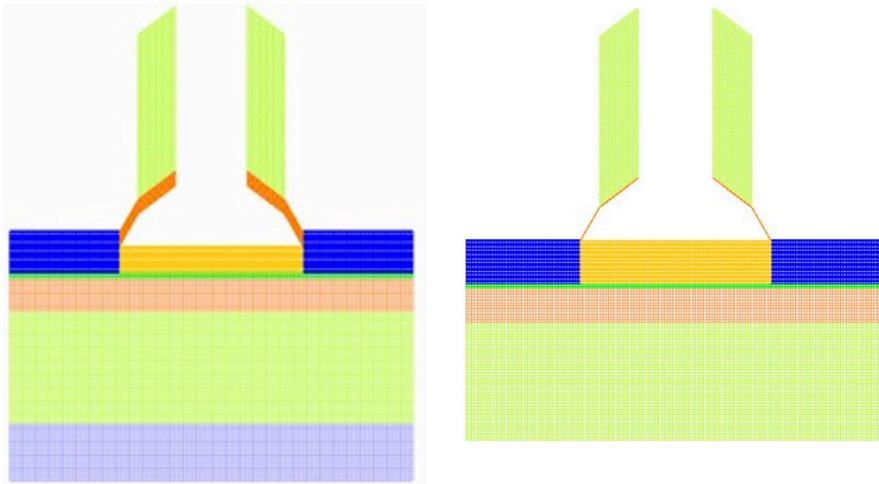
Figure 6. Computational grid arrangements; (CR= 3.5) □□ □ = 36⁰ and 360⁰

In Figure 7- Figure 8, the predictions of the velocity fields (velocity field and velocity magnitude) for test Case I are presented for both models. And, the turbulence intensity distributions for this test case are shown in Figure 9 & Figure 10.

The vector plots of velocity field for test Case II are shown in Figure 11 and 12 for both models.

The predictions of the axial mean velocity and turbulence intensity profiles of the standard k-□ and are compared with the experimental data in Figures 13 and Figures 14 for test Case I and Case II, respectively.
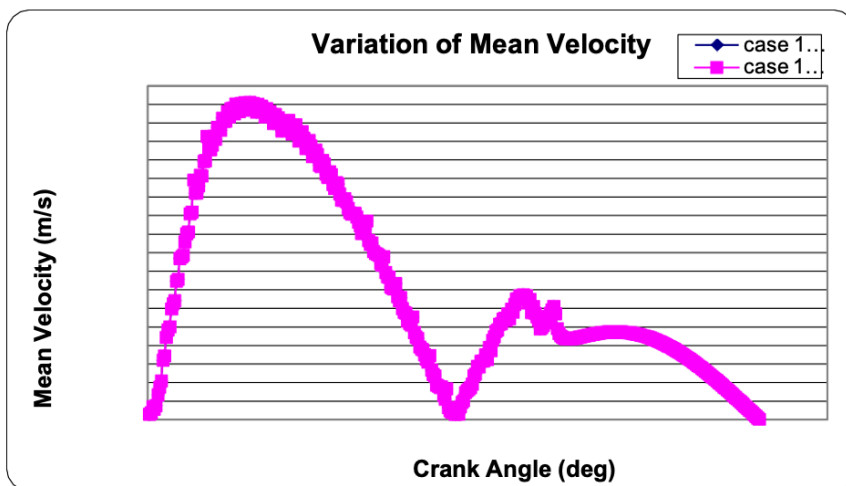

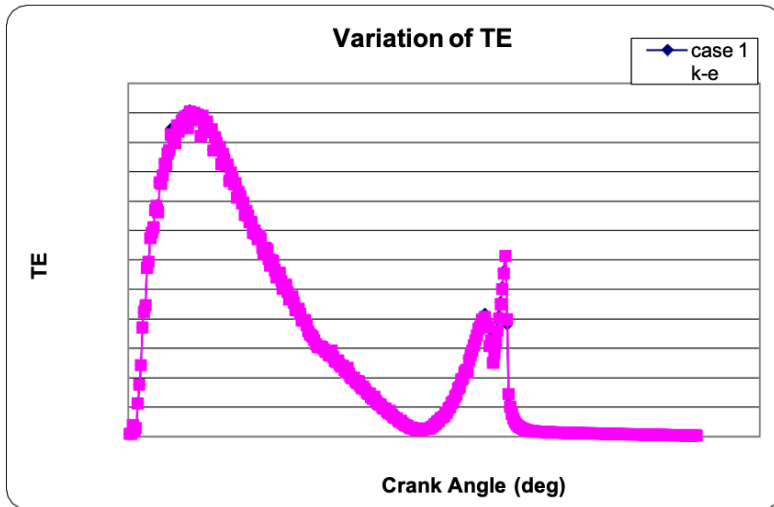**Figure 7.** Variation of Mean Velocity of the case I

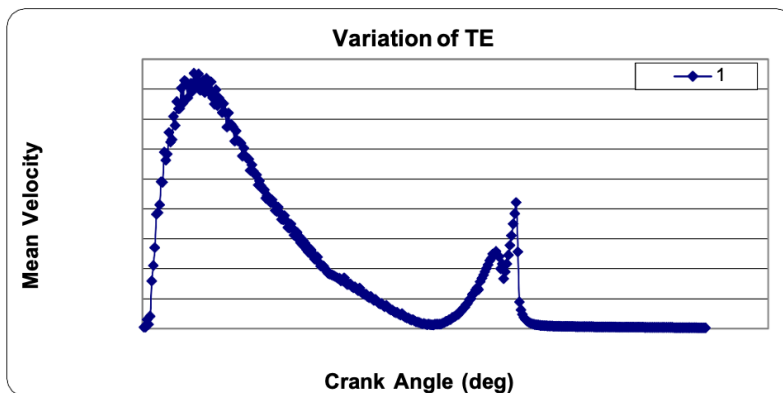**Figure 8.** Variation of Turbulence Energy of the case I

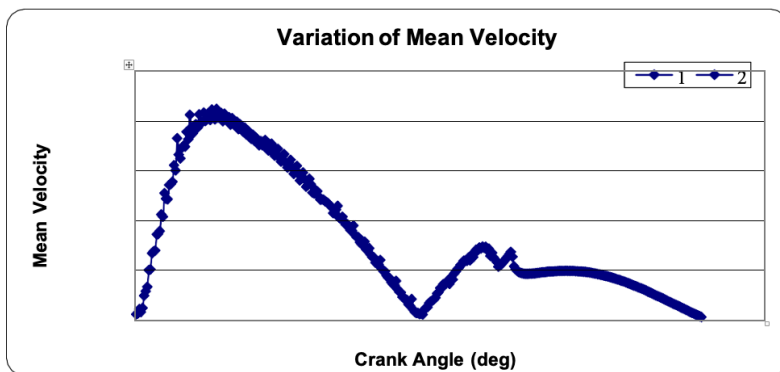**Figure 9.** Variation of Turbulence Energy of the Case II

Figure 10. Variation of Mean Velocity of the Case II

4. THE PREDICTIONS AND COMPARISONS FOR CASE I

The flow field during early stages of induction (for □=360 to 900 CA) can be seen can be seen from Figure 11 & Figure 12. Although appearing to undergo minor deflections, intake flow penetrates and impinges on the piston or cylinder wall, depending on the piston position. Then, it separates into two strong recirculation zones (vortex) oneof which is formed at the cylinder head-wall corner and the other is formed behind the inlet valve. Both vortices are toroidal. The center of both recirculation zones appears to be slightly more to left than those of the k-□ model. The centers of both recirculation zones move downstream towards the piston until mid-intake stroke; this movement is small in the former while the latter stretches and becomes the dominant one. In the induction angular range (□=180) the swirl motion increases proportionally with the valve opening, apart from the late stage.
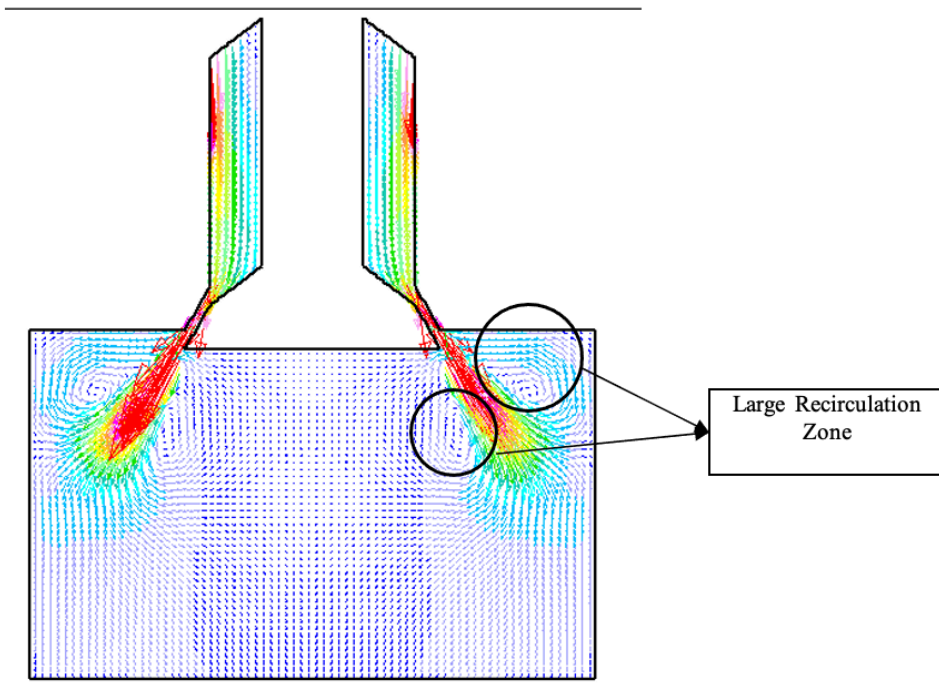

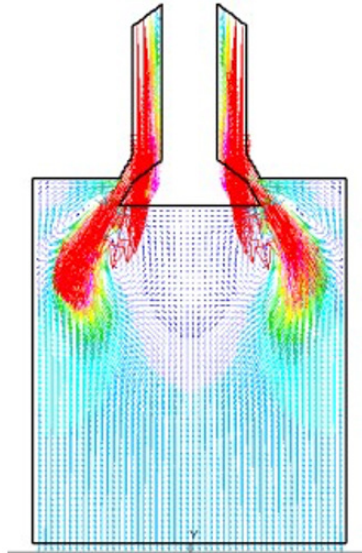**Figure 11.** Velocity field predictions of *the k-□* and RNG turbulence *model* for test Case I (□=36⁰CA)

Figure 12. Velocity field predictions of *the k-*□ and RNG turbulence *model* for test Case I at various crank angles in velocity contours and vector plots (□=90⁰CA)

The predicted and measured tangential velocity and turbulence kinetic energy of the mean value for the whole cycle are shown in Figure 12. However at early stages as CA=360 and 900 there is a better match between measured results. For turbulence kinetic energy, the predictions are much lower than the measured values in the region below the valves. At 15mm below the cylinder head the predicted flow structure is very similar to that of the laser sheet images as seen in Figure 12.

Two cases are performed with k-e and RNG turbulence model. The main differences noted for the RNG k-e turbulence model were slightly better resolution of recirculation zones and a merging of the large and small vortices at 15mm below the cylinder head into one large vortex. Comparisons of both models with the LDA Measurements indicate that the tangential velocity predictions are better for the k-e model and the turbulence kinetic energy predictions are better with the RNG k-e model, especially at early stages of induction . Overall, there was no significant benefit in using the RNG k-e model in preference to the k-e model and subsequent simulations retained the k-e model. During early intake stroke the turbulence intensity contours of Figure 12 suggest that the origin of induction generated turbulence lies mainly within the shear layers on

either side of the induction jet. Turbulence intensity contours have higher gradients at the centers of the recirculation zones and impingement points on the cylinder wall. Turbulence is then transported downstream towards the piston but its diffusion towards the cylinder axis is small, resulting in low levels of turbulence in the region of the valve wake.

5. COMPARISON OF RESULTS WITH THE EXPERIMENTAL DATA

Comparison of results with the experimental data will give more accurate assessment of suggested turbulence model. It was done by comparing the predictions of the normalized mean axial velocity of the k-e models, and RNG model, with the measurements. Figures 13-15 show these comparisons between RNG, k-e turbulence model and measurement values.
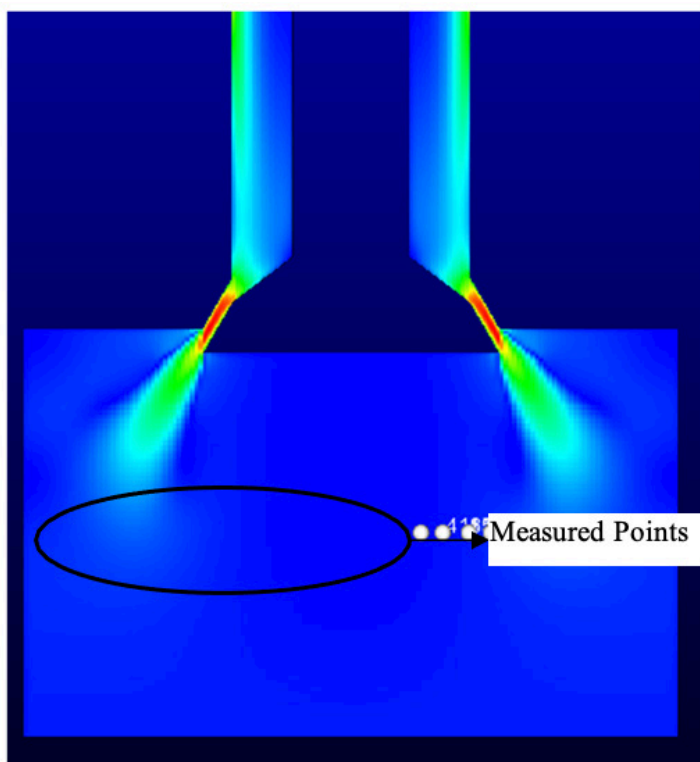

Figure 13. The comparison location z=15 mm for the two turbulence model

The measured and predicted radial profiles of the axial mean velocity and turbulence intensity at 36o are shown in Figure 14. The position of the peak in the radial velocity is well predicted by the k-□ and RNG model.
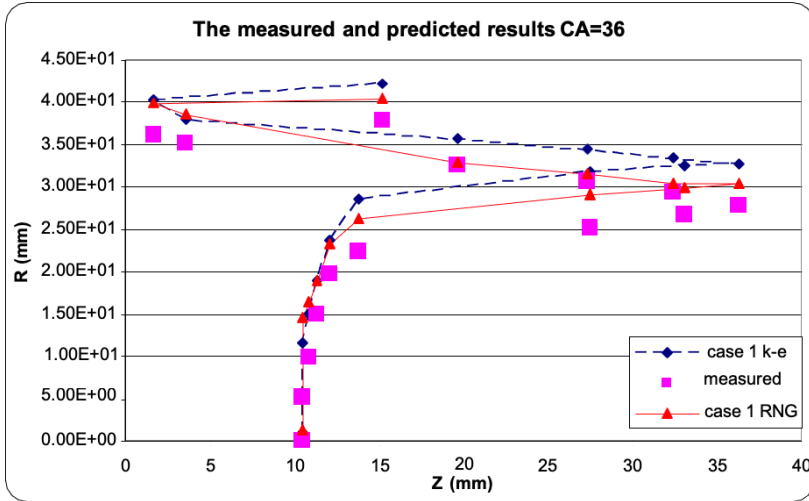
Figure 14. Comparison of Two Turbulence Model ($\square=36^0$CA)

The comparisons of corresponding profiles at 90o are shown in Figure 15. The stretching of the main vortex by the piston and an increase in its peak velocity together with an increase in the level of turbulence intensity are evident from Figure 15. The predictions of both models show similar trends. However, the positions of the peak velocities and their magnitude as well as the recirculation zone behind the valve are captured well by the RNG model than the k-$\square$ model. Turbulence intensities are also predicted better by the RNG model
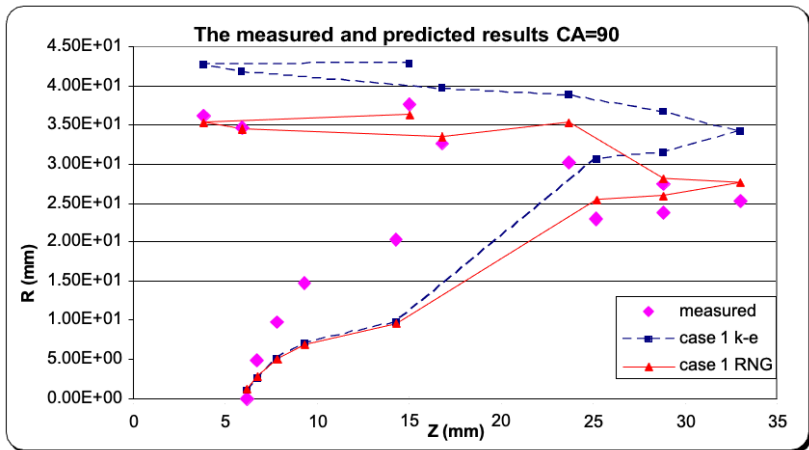

Figure 15. Comparison of two turbulence model for ($\square=90^0$CA)

In Figure 15 the prediction of the mean velocity profiles at 270o shows that the strength of the main vortex persisting from the induction is grossly over-predicted by both turbulence models. According to data, the mean flow at the measurement location (z=15mm) is almost one dimensional, in the direction of the piston motion, except for a weak vortex near the cylinder wall and the turbulence intensity has decayed to the level 0.75 times of piston mean velocity and is virtually homogeneous. For the turbulence intensities, the RNG model and the MM k-□ model show an over prediction, although the tendency towards homogeneity is well predicted.

6. CONCLUSION

A series of transient flow simulations have been performed for axsymmetry engine configurations for valve lifts. The simulations were conducted on computational meshes constructed by an automatic meshing procedure that is included events and reordering vertices. This procedure delivers a mesh in less than 15% of the time required by current meshing techniques.

In this study, effects of the two different turbulence model for in-cylinder engine flows are obtained and compare the general performance during induction and compression stroke of the engine simulator. The predicted flow structure, in-cylinder tangential velocity and turbulence were compared LDA velocity and turbulence measurements. The following conclusions are drawn from the comparison. Good qualitative and quantitative agreement between the predicted and measured in-cylinder flow was obtained for full strokes. Both the RNG and the k-□-models yield qualitatively similar behavior of the in-cylinder flow, but the RNG model produces better profiles in most of the locations where comparisons are made with the experimental data.

In the majority of cases the predicted in-cylinder turbulence levels were significantly lower than the measured values. Switching to an RNG k-e turbulence model resulted in only a minor improvement in the predicted turbulence levels. Because the RNG model damps main vortex more, giving better agreement for the mean velocities than the k-model during late compression stroke. Predicted turbulence intensities by the the k-□ model during this stage are in good agreement with the data.

REFERENCES

[1] W. Shyy, S.S.T., Computational Techniques for complex transported phenomena. New York, Cambridge, (1997)100-115

[2] Shyy W, U.H., Computational Fluid Dynamics with Moving Boundaries. Taylor and Francis, Washington DC. (1996) 116-125.

[3] Gul, M.Z.: "Prediction of In-Cylinder Flow by Use of a Multiple-Time-Scale Turbulence Model", PhD Thesis, Victory University of Manchester, (1994) 60-90.

[4] Wu, C.T., Ferziger, J.H; Chapman, D.R., Simulation and modeling of homogeneous, compressed turbulence. Fifth Symp. of Turbulent Shear Flows, Cornell Univ, (1985) 17.13-17.20.

[5] Hergart, C., Barths, H., and Peters, N., Modeling the Combustion Process in a Small-Bore Diesel Engine Using a Model Based on Representative Interactive Flamelets. SAE Technical Paper Series, (1999) 1999-01-3550.

[6] P., M., In-Cylinder Turbulent Flow Structure in Direct Injection, Swirl Supported Diesel Engines. (2003)

[7] Zhang, Y., A Numerical Study of In-Cylinder Mixture Formation in a Low Pressure Direct Injection Gasoline Engine, in Master Degree of Science. Michigan State University. (2007)

[8] Haworth, Multidimensional port-and-cylinder flow calculations for two and four valve-per-cylinder engines: influence of intake configuration on flow structure. SAE Technical Paper Series, (1990) p. 647-678.

[9] Heywood, J.B., Fluid motion within the cylinder of internal combustion engines- the 1986 freeman scholar lecture. . Journal of Fluids Engineering, (1987). 109: p. 3-35.

[10] Davis, G.C., Mikulec, A., Kent, Modeling the Effect of Swirl on Turbulence Intensity and Burn Rate in S.I.Engines and Comparison with Experiment. SAE Technical Paper Series, (1986)

[11] Witze, P.O., The Effect of Spark Location in Combustion in a Variable

Swirl Engines. SAE Technical Paper Series, (1982) 820044.

[12] Nagayama, I., Araki, Y., and Ioka, Y, Effects of Swirl and Squish on S.I. Engine Combustion and Emission. SAE Technical Paper Series, (1977)

[13] Drake M.C., H.D., Advanced gasoline engine development using optical diagnostics and numerical modeling Proceedings of a Symposium on Combustion (2007)

[14] Moureau V., B.I., Towards Large Eddy Simulation in ICE: simulations of a compressed tumble flow. SAE Technical Paper Series, (1994)

[15] Launder B.E., S., D.B., Mathematical Models of Turbulence. New York, Academic Press, (1972)